

AD-A061 241 MASSACHUSETTS INST OF TECH LEXINGTON LINCOLN LAB  
SOLID STATE RESEARCH, 1978:2.(U)  
MAY 78 A L MCWHORTER

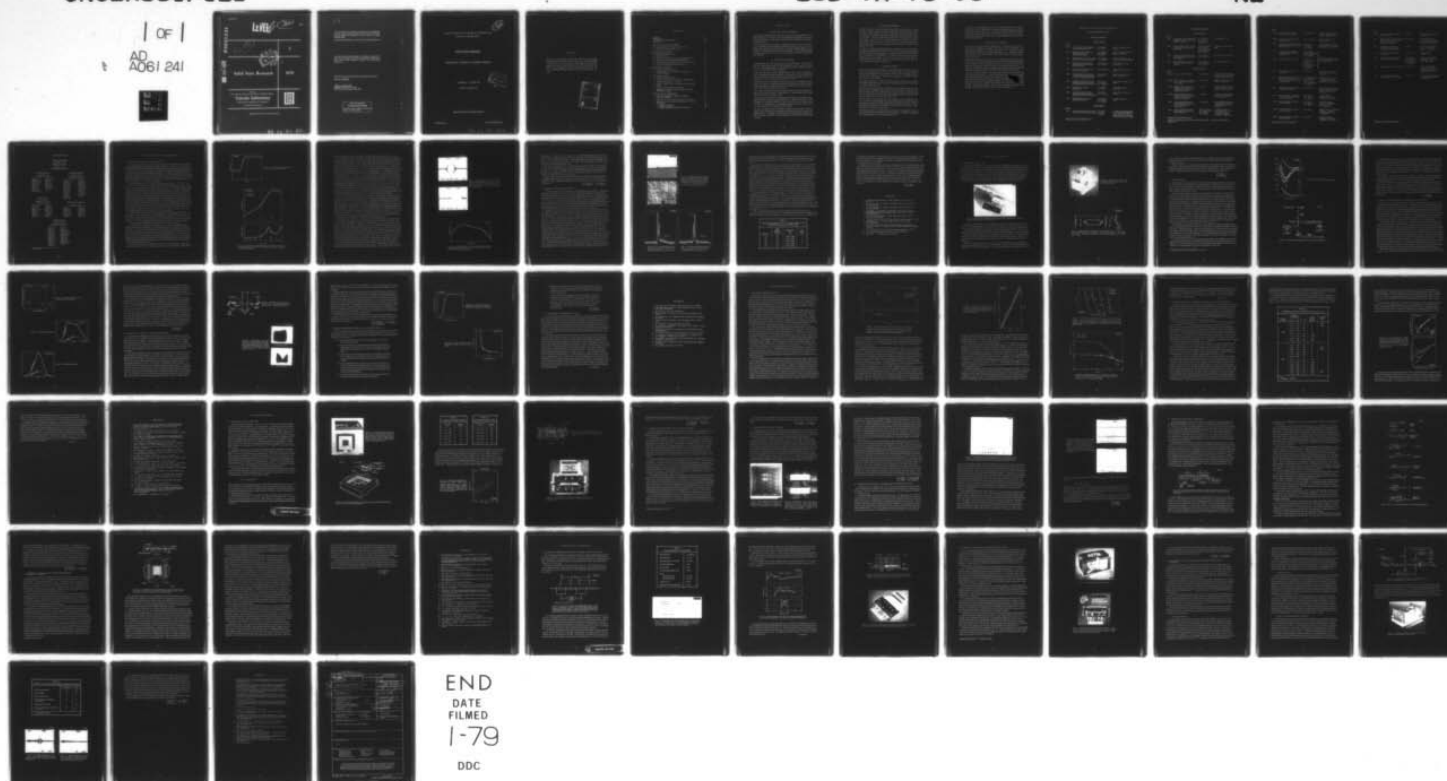
F/G 20/12

UNCLASSIFIED

ESD-TR-78-96

F19628-78-C-0002  
NL

| of |  
AD  
A061 241



**LEVEL**

*TD*

AD A061241

DDC FILE COPY

*Lee 1473*



2

**Solid State Research**

**1978**

Prepared  
under Electronic Systems Division Contract F19628-78-C-0002 by

**Lincoln Laboratory**

MASSACHUSETTS INSTITUTE OF TECHNOLOGY

LEXINGTON, MASSACHUSETTS



Approved for public release; distribution unlimited.

78 11 06 029

The work reported in this document was performed at Lincoln Laboratory, a center for research operated by Massachusetts Institute of Technology, with the support of the Department of the Air Force under Contract F19628-78-C-0002.

This report may be reproduced to satisfy needs of U.S. Government agencies.

The views and conclusions contained in this document are those of the contractor and should not be interpreted as necessarily representing the official policies, either expressed or implied, of the United States Government.

This technical report has been reviewed and is approved for publication.

FOR THE COMMANDER

*Raymond L. Loiselle*  
Raymond L. Loiselle, Lt. Col., USAF  
Chief, ESD Lincoln Laboratory Project Office

Non-Lincoln Recipients

**PLEASE DO NOT RETURN**

Permission is given to destroy this document  
when it is no longer needed.

12

MASSACHUSETTS INSTITUTE OF TECHNOLOGY  
LINCOLN LABORATORY

SOLID STATE RESEARCH

QUARTERLY TECHNICAL SUMMARY REPORT

1 FEBRUARY - 30 APRIL 1978

ISSUED 31 AUGUST 1978

DDC  
RECEIVED  
NOV 15 1978  
F

Approved for public release; distribution unlimited.

LEXINGTON

MASSACHUSETTS

78 11 06 029



ABSTRACT

This report covers in detail the solid state research work of the Solid State Division at Lincoln Laboratory for the period 1 February through 30 April 1978. The topics covered are Solid State Device Research, Quantum Electronics, Materials Research, Microelectronics, and Surface-Wave Technology. Funding is primarily provided by the Air Force, with additional support provided by the Army, ARPA, NSF, and DOE.

ACCESSION for	
NTIS	White Section <input checked="" type="checkbox"/>
DDC	Buff Section <input type="checkbox"/>
UNANNOUNCED	<input type="checkbox"/>
JUSTIFICATION	
BY	
DISTRIBUTION/AVAILABILITY CODES	
Dist	SPECIAL
A	

## CONTENTS

Abstract	iii
Introduction	vii
Reports on Solid State Research	x
Organization	xiv
 I. SOLID STATE DEVICE RESEARCH	 1
A. Gap-Coupled InSb/LiNbO <sub>3</sub> Convolver at 77 K.	1
B. Optically Pumped HgCdTe Lasers	5
 II. QUANTUM ELECTRONICS	 9
A. Hand-Held NdP <sub>5</sub> O <sub>14</sub> Laser	9
B. Mini-TEA Laser	11
C. Optical Energy Extraction From Molecular Mercury	13
D. Generation of Tunable Far-Infrared Radiation	15
E. Infrared Absorption Studies of CO <sub>2</sub> -Laser-Excited SF <sub>6</sub>	17
F. CO <sub>2</sub> -Laser-Induced Dissociation of SiH <sub>4</sub>	19
 III. MATERIALS RESEARCH	 21
A. Electrical Properties of InP	21
B. Liquidus Data for LPE Growth of Ga <sub>0.47</sub> In <sub>0.53</sub> As on InP Substrates	25
 IV. MICROELECTRONICS	 31
A. Monolithic Silicon Bolometers	31
B. Charge-Coupled Devices: SAW/CCD Buffer Memory	35
C. Charge-Coupled Devices: Imagers	36
D. Charge-Coupled Devices: Programmable Transversal Filter	37
E. Charge-Coupled Devices: Processing	40
F. Alignment of Liquid Crystals Using Submicrometer Periodicity Gratings	43
 V. SURFACE-WAVE TECHNOLOGY	 49
A. Filter With Bandwidth Continuously Variable From 3 to 100 MHz	49
B. Assembly of Gap-Coupled Acoustoelectric Devices	53
C. Development of an Acoustoelectric-Memory-Correlator Subsystem	55
1. Mechanical Structure	55
2. LiNbO <sub>3</sub> Delay Line	56
3. Memory-Correlator-Subsystem Performance	56

## INTRODUCTION

### I. SOLID STATE DEVICE RESEARCH

A gap-coupled InSb/LiNbO<sub>3</sub> acoustoelectric convolver has been operated at 77 K with an efficiency of -63 dBm. This result suggests the possibility of using a high-density InSb-diode-array/LiNbO<sub>3</sub> structure as an acoustically scanned infrared imaging device.

CW laser operation with an emission wavelength of 2.79  $\mu\text{m}$  has been achieved at  $\sim 12$  K in optically pumped liquid-phase epitaxially grown  $\text{Hg}_{0.557}\text{Cd}_{0.443}\text{Te}$ . Also, pulsed laser action has been observed at 77 K upon optically pumping various HgCdTe LPE samples with a Q-switched Nd:YAG laser. The stimulated emission wavelength varied from 1.25 to 2.97  $\mu\text{m}$  as the mole fraction of CdTe changed from 0.729 to 0.410.

### II. QUANTUM ELECTRONICS

A self-contained, hand-held  $\text{NdP}_5\text{O}_{14}$  laser has been fabricated. The laser head assembly of flash lamp, laser rod, and pump radiation collector has a volume of 1.5  $\text{cm}^3$ . Without optimization, this unit presently provides  $\sim 1000$  laser shots of 0.5 mJ at 1.06  $\mu\text{m}$  between battery chargings.

A mini-TEA CO<sub>2</sub> laser has been operated with a "three-mirror" grating-tuned cavity and single-line tunability obtained in both the 10.6- and 9.4- $\mu\text{m}$  branches. The mini-TEA laser has also achieved arc-free operation at pulse repetition frequencies up to 250 Hz and an average output power of 3.6 W.

An effort is under way to efficiently extract energy from the metastable levels of the mercury excimer. Experiments have been conducted which measure the wavelength, temperature, and density dependencies of infrared-laser-induced enhancement of the excimer fluorescence near 330 nm.

The recently developed GaAs Schottky-diode mixer has been used to generate tunable CW far-infrared radiation. Demonstration of high-resolution spectroscopy using this source has been made on D<sub>2</sub>O.

The time scale of intramolecular vibrational energy transfer has important consequences for bond-selective infrared photochemistry. Measurements of the  $\nu_3$ -band absorption of CO<sub>2</sub>-laser-excited SF<sub>6</sub> have been carried out at fluences up to 1 J/cm<sup>2</sup>. A redistribution of the vibrational energy takes place on a several-microsecond time scale, independent of SF<sub>6</sub> pressure.

The CO<sub>2</sub> TEA-laser induced dissociation of silane has been studied in order to improve the understanding of multiphoton excitation processes in unimolecular photochemistry. In contrast to SF<sub>6</sub>, dissociation of SiH<sub>4</sub> requires pressures of a few Torr and is accompanied by visible luminescence from atomic and molecular hydrogen.



### III. MATERIALS RESEARCH

Resistivity and Hall coefficient measurements have been made on numerous n-type (undoped, Sn-doped), p-type (Zn-doped, Cd-doped), and semi-insulating (Fe-doped) InP single crystals grown by the liquid-encapsulated Czochralski method to provide substrates for epitaxial growth of GaInAsP alloys for infrared diode lasers and detectors. For the Fe-doped sample with lowest room-temperature carrier concentration ( $n = 1.2 \times 10^7 \text{ cm}^{-3}$ ), the room-temperature resistivity and Hall mobility are  $1.6 \times 10^8 \text{ } \Omega\text{-cm}$  and  $3.3 \times 10^3 \text{ cm}^2 \text{ V}^{-1} \text{ sec}^{-1}$ , respectively, and the activation energy determined by measuring the Hall coefficient as a function of temperature is 0.65 eV.

In a study of the liquid-phase epitaxial growth of GaInAs layers on InP substrates, the liquidus compositions and temperatures have been determined for deposition of the lattice-matched alloy  $\text{Ga}_{0.47}\text{In}_{0.53}\text{As}$ , a material of interest for infrared diode lasers, photodiodes, and photocathodes. To obtain this alloy with a given As concentration in the growth solution, the Ga concentration in the solution and the liquidus temperature must both be higher for (111)B substrates than for (100) substrates at growth temperatures below 690°C.

### IV. MICROELECTRONICS

Silicon bolometers etched from single-crystal silicon wafers are being developed for use as broadband detectors in the 1- to 30- $\text{cm}^{-1}$  band. The first detectors have noise equivalent powers of a few times  $10^{-14} \text{ W/Hz}^{1/2}$  with single time constants of a few milliseconds, compared with a design goal of  $2 \times 10^{-15} \text{ W/Hz}^{1/2}$  with a 1/30-sec time constant.

A packaging technique for a SAW/CCD buffer memory device has been developed which allows mating the silicon chip with its sampling fingers and CCD structure to a lithium niobate delay line.

The first two-chip arrays of 100- $\times$ 400-element CCD imaging devices have been fabricated for the GEODSS Program and will be used to test the optical moving target indicator (MTI) system for automatic satellite detection. Recent tests on the 100- $\times$ 400-element CCD chips have shown that the measured dark current has been made as low as 6 nA/ $\text{cm}^2$  over the entire device.

Matched filtering has been performed with a prototype device consisting of two 1-bit, 32-tap CCD programmable transversal filter sections which are capable of performing correlation of analog-sampled data with a binary reference. The programmable binary reference code of these devices is stored in an on-chip, serial-in/parallel-out n-MOS static shift register.

A processing sequence for the fabrication of two-phase, buried-channel CCDs has been developed which is compatible with the fabrication of n-MOSFETs having high punch-through voltages and low back-gate-bias effects.



To produce uniform alignment of the director in nematic and smectic liquid-crystal layers, 320-nm spatial-period square-wave gratings fabricated on amorphous  $\text{SiO}_2$  substrates were used. This demonstrates that molecular alignment can be achieved using surface structures fabricated by a planar process. A novel method of producing twisted-nematic liquid-crystal displays using surface gratings has been demonstrated.

## V. SURFACE-WAVE TECHNOLOGY

A filter has been developed whose bandwidth can be continuously varied over a range from 3 to 100 MHz by changing the frequency of a CW control signal. This filtering system exploits the extremely sharp skirts ( $-3$  to  $-40$  dB in 3.5 MHz) achievable with reflective-array-compressor (RAC) devices. Amplitude response, phase response, out-of-band rejection, and dynamic range of the filter system have been measured.

A specialized assembly procedure has been developed for gap-coupled acoustoelectric devices consisting of a  $\text{LiNbO}_3$  delay line and a silicon strip separated by an intervening air gap. Air gaps of the order of 0.2 to 0.6  $\mu\text{m}$  can be accurately obtained and held uniform to within  $\pm 0.02$   $\mu\text{m}$  over lengths as large as 7 cm. The procedure achieves this goal by maintaining extreme cleanliness while employing specialized mountings and jigs for accurately assembling the separate parts.

A memory-correlator subsystem with a bandwidth of 60 MHz and correlation length of 5  $\mu\text{sec}$  has been developed. The key element of the subsystem is an improved acoustoelectric memory correlator which functions as a programmable matched filter. Improvements include the use of a spacer-rail support structure to control transverse modes, the use of multistrip couplers to reduce spurious surface-wave signals, and the use of a balanced transformer feed to reduce direct EM feed-through. The required interfaces, drive circuits, and output circuits have been developed and incorporated in the memory-correlator subsystem.

# REPORTS ON SOLID STATE RESEARCH

15 February through 15 May 1978

## PUBLISHED REPORTS

### Journal Articles

<u>JA No.</u>			
4710	Micro-Fresnel Zone Plates for Coded Imaging Applications	N. M. Ceglio* H. I. Smith	Rev. Sci. Instrum. <u>49</u> , 15 (1978)
4746	Spectroscopy and Lasing of a High Nd Concentration Al-Phosphate Glass	A. Lempicki* R. M. Klein* S. R. Chinn	IEEE J. Quantum Electron. <u>QE-14</u> , 283 (1978)
4784	High-Resistivity Layers in n-InP Produced by Fe Ion Implantation	J. P. Donnelly C. E. Hurwitz	Solid-State Electron. <u>21</u> , 475 (1978), DDC AD-A053929
4786	Collisionless Intramolecular Energy Transfer in Vibrationally Excited SF <sub>6</sub>	T. F. Deutsch S. R. J. Brueck	Chem. Phys. Lett. <u>54</u> , 258 (1978)
4793	1-mJ, Line-Tunable Optically Pumped 16 μm Laser	R. M. Osgood, Jr.	Appl. Phys. Lett. <u>32</u> , 564 (1978)
4801	Efficient Phase-Matched Infrared Third-Harmonic Generation in Liquid CO <sub>2</sub> -SF <sub>6</sub> Mixtures	S. R. J. Brueck H. Kildal	Opt. Lett. <u>2</u> , 33 (1978), DDC AD-A054569
4802	Simplified Fabrication of GaAs Homojunction Solar Cells with Increased Conversion Efficiencies	J. C. C. Fan C. O. Bozler R. L. Chapman	Appl. Phys. Lett. <u>32</u> , 390 (1978)
4808	GaInAsP/InP Avalanche Photodiodes	C. E. Hurwitz J. J. Hsieh	Appl. Phys. Lett. <u>32</u> , 487 (1978)
4810	Oriented Crystal Growth on Amorphous Substrates Using Artificial Surface-Relief Gratings	H. I. Smith D. C. Flanders	Appl. Phys. Lett. <u>32</u> , 349 (1978)
4830	Proton Bombardment: For Making GaAs Devices	J. P. Donnelly C. O. Bozler R. A. Murphy	Circuits Mfg. <u>18</u> , 45 (1978)

### Meeting Speech

<u>MS No.</u>			
4415	Ternary Semiconductor Crystals for Nonlinear Optical Applications	G. W. Iseler H. Kildal N. Menyuk	In <u>Ternary Compounds, 1977</u> , Conf. Ser. No. 35, edited by G. D. Holah (The Institute of Physics, Bristol and London, 1977), p. 73, DDC AD-A054566

---

\* Author not at Lincoln Laboratory.

# UNPUBLISHED REPORTS

## Journal Articles

JA No.			
4776	Explanation of the 6-fold LEED Patterns from Polar (0001) and (000 $\bar{1}$ ) ZnO Surfaces	V. E. Henrich H. J. Zeiger E. I. Solomon* R. R. Gay	Accepted by Surf. Sci.
4797	Magneto-Optical Study of Shallow Donors in Transmutation Doped GaAs	J. H. M. Stoelinga* D. M. Larsen* W. Walukiewicz* R. L. Aggarwal* C. O. Bozler	Accepted by J. Phys. Chem. Solids
4803	Vibrational Energy Relaxation and Exchange in Liquid N <sub>2</sub> -CO-OCS Mixtures	S. R. J. Brueck R. M. Osgood, Jr.	Accepted by J. Chem. Phys.
4811	Surface Defects and the Electronic Structure of SrTiO <sub>3</sub> Surfaces	V. E. Henrich G. Dresselhaus H. J. Zeiger	Accepted by Phys. Rev. B

## Meeting Speeches<sup>†</sup>

MS No.			
4140G	Photoelectrolysis of Water	J. G. Mavroides	Physics Seminar, Dalhousie University, Halifax, Nova Scotia, Canada, 1 March 1978
4270B	Electron Spectroscopy of Surfaces: Defects on Transition-Metal Oxides	V. E. Henrich	Materials Science Seminar, M.I.T., 7 April 1978
4447A	Doppler-Limited Infrared Molecular Spectroscopy with a Tunable-Laser Difference-Frequency Converter	A. S. Pine	Seminar, National Research Council of Canada, Ottawa, Ontario, 27 March 1978
4447B	Doppler-Limited Infrared Molecular Spectroscopy with a Tunable-Laser Difference-Frequency Converter	A. S. Pine	Seminar, National Bureau of Standards, Washington, DC, 25 April 1978
4581A	The Electronic Structure of Transition-Metal-Oxide Surfaces: Defect States in Chemisorption	V. E. Henrich	Quantum Physics Seminar, Francis Bitter National Magnet Laboratory, M.I.T., 5 April 1978
4584	Advances in Schottky Diode Receivers and Planar GaAs Diode Detectors	H. R. Fetterman P. E. Tannenwald B. J. Clifton R. A. Murphy	Third Intl. Conf. on Submillimeter Waves and Their Applications, Guildford, England, 29 March - 1 April 1978

\* Author not at Lincoln Laboratory.

† Titles of Meeting Speeches are listed for information only. No copies are available for distribution.

MS No.

4584A	Schottky Diodes and their Application to Spectroscopy	H. R. Fetterman	Seminar, Francis Bitter National Magnet Laboratory, M.I.T., 3 May 1978
4588A	Acoustically Scanned Optical Imaging Devices	F. J. Leonberger	Optics Seminar, M.I.T., 8 March 1978
4608	Spectroscopic Studies of Small Molecule Intermediates on Metal Oxide Surfaces	R. R. Gay E. I. Solomon* V. E. Henrich H. J. Zeiger	175th Meeting, American Chemical Society, Anaheim, California, 16 March 1978
4635	Temperature and Magnetic Field Dependence of Nickel Carbonylation	M. S. Mehta* M. S. Dresselhaus* G. Dresselhaus* H. J. Zeiger	American Physical Society Meeting, Washington, DC, 27-30 March 1978
4640	Lattice Modes of Fresnoite	T. Chieu* G. Dresselhaus* K. Ho* L. Schmutz* R. Silberstein* C. Underhill* T. B. Reed	
4655	Electron Beam and X-ray Lithography	H. I. Smith	SPIE 31st Annual Conf., Washington, DC, 30 April - 5 May 1978
4664	High Power Laser and Low Noise Receiver for Submillimeter Thomson Scattering Ion Temperature Diagnostic	P. Woskoboinikow* H. C. Praddaude* D. R. Cohn* H. R. Fetterman P. E. Tannenwald B. J. Clifton	2nd Topical Conf. on High Temperature Plasma Diagnostics, Santa Fe, New Mexico, 1-3 March 1978
4665	Signal Processing with CCD's - A Complement to SAW's	A. M. Chiang	Boston Section IEEE Group on Sonics and Ultrasonics, Bedford, Massachusetts, 15 March 1978
4689	New Applications of Submicrometer Structures in Material Science and Biology	H. I. Smith D. C. Flanders D. C. Shaver	Scanning Electron Microscopy 1978, Los Angeles, 17-21 April 1978
4689A	New Applications of Submicrometer Structures	H. I. Smith D. C. Flanders D. C. Shaver	Cornell University Submicron Colloquium, Ithaca, New York, 23 February 1978
4689B	New Applications of Submicrometer Structures	H. I. Smith	Applied Physics Colloquium, California Institute of Technology, Pasadena, 19 April 1978
4689C	New Applications of Submicrometer Structures	H. I. Smith	Stanford University Colloquium, Palo Alto, California, 20 April 1978

\* Author not at Lincoln Laboratory.



MS No.

4689D	New Applications of Submicro-meter Structures	H. I. Smith	IBM, San Jose, California, 21 April 1978
4691	High Sensitivity, 1.4 GHz Bandwidth 12-Element HgCdTe Photodiode Arrays for 10.6 $\mu$ m Heterodyne Detection	D. L. Spears	26th National Infrared Information Symp., Air Force Academy, Colorado Springs, 9-11 May 1978
4709	Analog Signal Processing with Surface Acoustic Wave and Charge-Coupled Devices	E. Stern	IEEE Group on Electron Devices, Pittsburgh Chapter, 22 March 1978
4713	Neodymium Pentaphosphate Mini-Lasers	S. R. Chinn	Seminar, M.I.T., 12 April 1978
4729	Donor Spectra of High Purity Transmutation Doped GaAs	D. M. Larsen* J. H. Stoelinga* W. Walukiewicz* R. L. Aggarwal* C. O. Bozler	Neutron Transmutation Doping Conf., University of Missouri, Rolla, 23-26 April 1978
4739	Photodetectors for Fiber Optics	C. E. Hurwitz	Symp. on Components for Future EW Systems, MITRE Corporation, Bedford, Massachusetts, 11 May 1978
4950	Selective-Black Absorbers Using Sputtered Cermet Films	J. C. C. Fan	Intl. Conf. on Metallurgical Coatings, San Francisco, 3-7 April 1978

---

\* Author not at Lincoln Laboratory.

## ORGANIZATION

### SOLID STATE DIVISION

A. L. McWhorter, *Head*  
 I. Melngailis, *Associate Head*  
 C. R. Grant, *Assistant*  
 R. H. Kingston, *Senior Staff*  
 P. E. Tannenwald, *Senior Staff*

### QUANTUM ELECTRONICS

A. Mooradian, *Leader*  
 P. L. Kelley, *Associate Leader*

Barch, W. E.	Fleming, M. W.*
Belanger, L. J.	Hancock, R. C.
Blumberg, W. A. M.	Kildal, H.
Brueck, S. R. J.	Menyuk, N.
Burke, J. W.	Moulton, P. F.
Chinn, S. R.	Osgood, R. M.
DeFeo, W. E.	Parker, C. D.
Deutsch, T. F.	Peck, D. D.
Ehrlich, D. J.	Pine, A. S.
Fetterman, H. R.	

### ELECTRONIC MATERIALS

A. J. Strauss, *Leader*  
 H. J. Zeiger, *Associate Leader*  
 J. G. Mavroides, *Senior Staff*

Anderson, C. H., Jr.	Hsieh, J. J.
Bayard, M. L.	Iseler, G. W.
Button, M. J.	Kafalas, J. A.
Cava, R. J.*	Kolesar, D. F.
Chapman, R. L.	Krohn, L., Jr.
Davis, F. M.	Mastromattei, E. L.
Delaney, E. J.	Owens, E. B.
Fahey, R. E.	Palm, B. J.
Fan, J. C. C.	Pantano, J. V.
Feldman, B.	Smith, D. D.
Finn, M. C.	Tchernev, D. I.
Gay, R. R.*	Tracy, D. M.
Henrich, V. E.	Vohl, P.
Hong, H. Y-P.	

### APPLIED PHYSICS

A. G. Foyt, *Leader*  
 C. E. Hurwitz, *Assistant Leader*  
 T. C. Harman, *Senior Staff*

Armiento, C. A.*	Groves, S. H.
Calawa, A. R.	Leonberger, F. J.
Carter, F. B.	Lind, T. A.
DeMeo, N. L., Jr.	McBride, W. F.
Diadiuk, V.*	Paladino, A. E.
Donnelly, J. P.	Plonko, M. C.
Duffy, P. E.	Spears, D. L.
Ferrante, G. A.	Tsang, D. Z.*
Glasser, L. A.*	Walpole, J. N.

### SURFACE WAVE TECHNOLOGY

E. Stern, *Leader*  
 R. C. Williamson, *Associate Leader*

Baker, R. P.	LaFleur, W. J.
Brogan, W. T.	Melngailis, J.
Cafarella, J. H.	Oates, D. E.
Dolat, V. S.	Ralston, R. W.
Holtham, J. H.	Reible, S. A.
Hurlburt, D. H.	Schulz, M. B.
Kernan, W. C.	Slattery, R. L.

### MICROELECTRONICS

W. T. Lindley, *Leader*  
 F. J. Bachner, *Associate Leader*  
 H. I. Smith, *Assistant Leader*

Alley, G. D.	Grant, L. L.
Beatrice, P. A.	Gray, R. V.
Bozler, C. O.	Hansell, G. L.*
Burke, B. E.	Hawryluk, A. M.*
Chiang, A. M.	Lincoln, G. A., Jr.
Clifton, B. J.	McGonagle, W. H.
Clough, T. F.	Mountain, R. W.
Daniels, P. J.	Murphy, R. A.
DeGraff, P. D.	Pichler, H. H.
Durant, G. L.	Shaver, D. C.*
Efremow, N., Jr.	Silversmith, D. J.
Felton, B. J.	Smythe, D. L., Jr.
Flanders, D. C.	Wilde, R. E.
Geis, M. W.	

\* Research assistant

## 1. SOLID STATE DEVICE RESEARCH

### A. GAP-COUPLED InSb/LiNbO<sub>3</sub> CONVOLVER AT 77 K

In a previous report,<sup>1</sup> the use of a gap-coupled Si-diode-array/LiNbO<sub>3</sub> memory correlator as an acoustically scanned imaging device (ASID) was discussed. One of the unique features of the ASID is the ability to employ surface-wave signal-processing techniques to an imaging device in real time. The device could thus be useful in special-purpose imaging applications such as Fourier-transform imaging and pattern recognition. The ASID is potentially useful as a solid state infrared imager if the silicon were replaced by an infrared diode array. To that end, preliminary experiments using InSb have been performed to demonstrate that an adequate acoustoelectric convolution efficiency can be achieved at 77 K with a gap-coupled InSb/LiNbO<sub>3</sub> structure. An efficiency of -63 dBm has been obtained.

For these experiments, 15-mil-thick low-concentration n-type ( $n \approx 1 \times 10^{14} \text{ cm}^{-3}$ ,  $\mu_{77} = 6 \times 10^5 \text{ cm}^2/\text{V-sec}$ ) InSb was used. Samples were processed to passivate the surface so that the zero-bias surface potential was near flat-band. This passivation was necessary so that the range of surface potentials corresponding to a depleted surface (i.e., the range of the highest convolution efficiency) could be accessed by biasing the InSb/LiNbO<sub>3</sub> structure. (If the InSb surface at zero bias is heavily accumulated or inverted, a low convolution efficiency will be obtained due to screening and attenuation effects.) The InSb samples were initially processed by electropolishing the surface and then growing a 400-Å-thick protective anodic oxide. The surfaces were passivated by stripping the anodic oxide with buffered HF, rinsing in DI water and alcohol, and then sequentially depositing 1000 Å of pyrolytic phosphosilicate glass (PSG) at 250°C and 1000 Å of sputtered SiO<sub>2</sub>. Details of the initial processing and the insulator deposition are given in Refs. 2 and 3, respectively. Layers of Au and Pt, each 1000 Å thick, were sequentially electroplated on the back side of the sample. Finally, the wafer was sawed to 66-mil widths appropriate for mounting in the convolver packages.<sup>4</sup>

The InSb surface potential was evaluated by making C-V measurements on MIS devices. These devices were formed by filament-evaporating Au top contacts through a mask over the SiO<sub>2</sub> surface. Measurements were made by probing at 500 kHz and 77 K. A C-V plot for a device formed from the same wafer that was used for the convolution measurements is shown in Fig. 1-1. From the calculated flat-band capacitance of the device, a flat-band voltage of -1.75 V was estimated, indicating that the surface is accumulated at zero bias.

For acoustoelectric measurements, an InSb strip ~1.4 cm long was indium-bonded to a Kapton strip and assembled against a LiNbO<sub>3</sub> delay line that had a pseudorandom array of ion-etched 5 μm-diam posts to maintain a 1500-Å gap between the InSb and LiNbO<sub>3</sub> surfaces. Details of the assembly procedure and of the convolver package are given in Ref. 4 and in Sec. V-B of this report. In order to maintain the gap uniformity at 77 K, the layer of RTV rubber (located between the Kapton and the spring components) used for room-temperature measurements was replaced by a cloth strip. Also, hermetic connectors were used and the package was purged and backfilled with helium to inhibit condensation that could otherwise occur on the delay-line surface at 77 K.

The convolution efficiency  $F$  and insertion loss  $L$  were measured with 70-MHz surface acoustic waves. Here,  $F = 10 \log(P_3/P_1 P_2)$ , where  $P_3$  is the convolution output signal

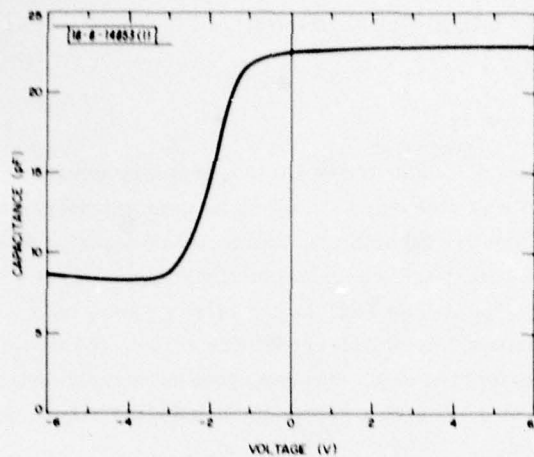


Fig. I-1. Capacitance-voltage plot at 77 K and 500 kHz for InSb MIS device.

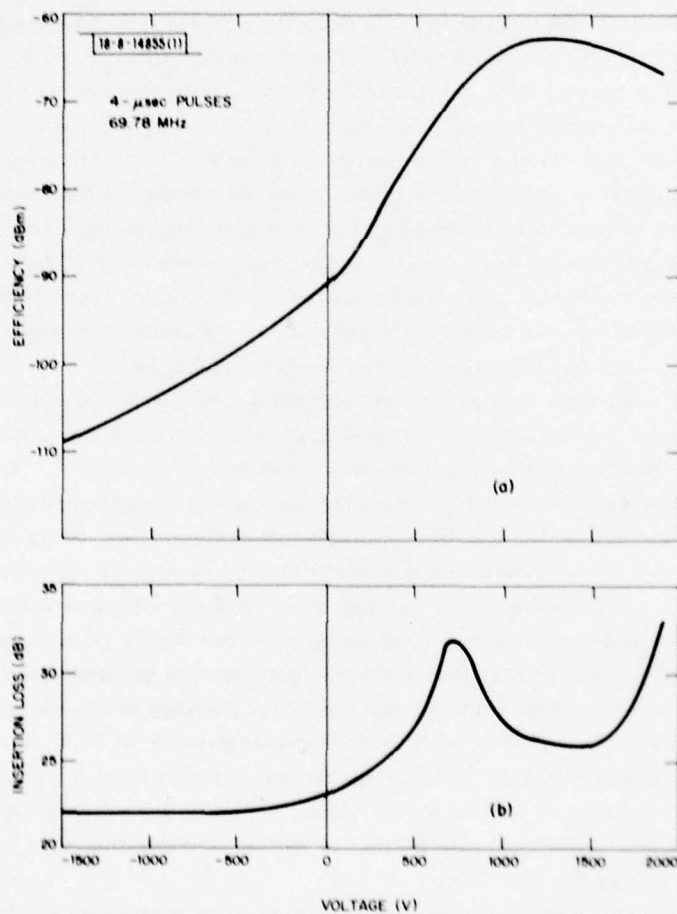


Fig. I-2. (a) Conversion efficiency and (b) insertion loss vs bias for InSb/LiNbO<sub>3</sub> convolver at 77 K. Negative voltages correspond to accumulation biases.



power and  $P_1$  and  $P_2$  are the signal powers applied to the two input transducers. Also,  $i = 10 \log (P_1/P_{20})$ , where  $P_1$  is the power applied to one transducer and  $P_{20}$  is the amount of that power extracted from the other transducer after the acoustic wave has traversed the length of the  $\text{InSb}/\text{LiNbO}_3$  structure. Acoustic pulse lengths of 4  $\mu\text{sec}$  (comparable to the acoustic transit time of the sample) were used. Measurements were made as a function of bias voltage  $V$ . The bias was applied to the structure between the convolver output port (i.e., the  $\text{InSb}$  back contact) and the  $\text{LiNbO}_3$  ground plane. Most (~99 percent) of the applied voltage was dropped across the 28-mil-thick  $\text{LiNbO}_3$  and the air gap. At room temperature,  $F = -110$  dBm and  $L = 24$  dB. These values were independent of bias because of the high intrinsic carrier density of  $\text{InSb}$  at room temperature ( $n_i \approx 4 \times 10^{15} \text{ cm}^{-3}$ ). The variation of  $F$  and  $L$  with bias at 77 K is shown in Figs. 1-2(a) and (b). The measurements were made by submerging the convolver in liquid  $\text{N}_2$ . For negative bias, the surface is accumulated and, as shown in Fig. 1-2(a),  $F$  is relatively low ( $< -91$  dBm). Note that the voltage polarity is reversed from that of the C-V measurements due to the package bias arrangement. As  $V$  becomes positive, the  $\text{InSb}$  surface first approaches flat-band potential and then becomes depleted. The efficiency increases, peaking at  $-63$  dBm for  $V \sim 1300$  V, and then decreases with larger biases as the surface becomes inverted. The insertion loss is shown in Fig. 1-2(b) and includes the 15-dB loss of the  $\text{LiNbO}_3$  delay line.  $L$  is relatively constant at 22 dB for accumulation biases, has a peak near flat-band, then decreases for small inversion biases, and finally increases again for large inversion biases.

To discuss the results shown in Figs. 1-2, it is useful to consider the loss effects first. The variation of  $L$  with bias can probably be attributed to transverse moding and scattering effects as well as changes in the surface resistivity  $\rho_s$ . Calculations indicate that for accumulation and depletion bias, losses should be negligible since the  $\text{InSb}$  has a 77-K resistivity of  $0.1 \Omega\text{-cm}$ . The 7-dB excess loss (over that for the  $\text{LiNbO}_3$  delay line) for accumulation biases is probably due to moding and scattering effects<sup>5</sup> associated with the loading of the ion-etched  $\text{LiNbO}_3$  posts by the  $\text{InSb}$  sample. The peak in  $L$  near flat-band and its decrease for depletion biases may be attributed to moding effects dependent on the effective gap width. The increase in  $L$  as the surface becomes inverted (i.e.,  $V \geq 1500$  V) is probably the rising edge of a peak attributable to acoustoelectric loss. This peak occurs because acoustoelectric loss is maximum for a value of  $\rho_s$  intermediate between that for a depleted and fully inverted surface.<sup>6</sup>

The variation of  $F$  with bias is quite similar to that observed for Si at room temperature and is attributable to changes in resistivity with bias near the semiconductor surface.<sup>6</sup> The surface carrier concentration is large for accumulation biases, and  $F$ , which is inversely proportional to the square of the concentration, is low. As flat-band potential is approached, the surface carrier concentration decreases, producing an increase in  $F$ . As bias is increased in depletion, the effective gap between the  $\text{LiNbO}_3$  surface and the depletion layer edge increases. This results in a reduced coupling to the semiconductor, but a more complete depth modulation in the semiconductor by the rf acoustoelectric field which further increases  $F$ . For weak inversion biases, the large increase in acoustoelectric loss causes a corresponding decrease in  $F$ . The estimated flat-band efficiency is within about 15 dB of that calculated from a computer model. The discrepancy is probably due to the excess delay-line losses discussed above.

A typical output convolution signal for equal-amplitude 4- $\mu\text{sec}$  surface-wave pulses is shown in Fig. 1-3(a) for the optimum bias of 1290 V. The  $-63$ -dBm efficiency shown is comparable to that measured on a Si-diode-array/ $\text{LiNbO}_3$  ASID. The uniformity of the convolution

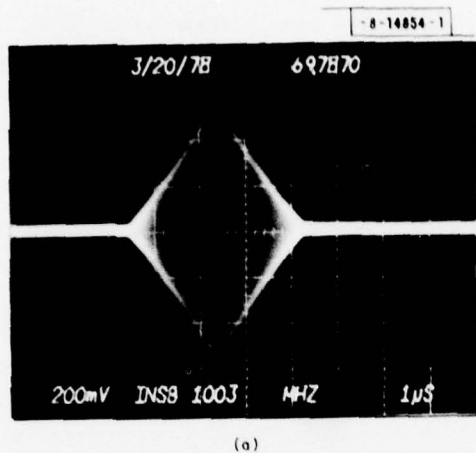


Fig.1-3. (a) Convolution output for 4- $\mu$ sec equal-amplitude pulses at 77 K and a 1290-V bias for InSb/LiNbO<sub>3</sub> device. (b) Corresponding convolution output uniformity for a 7- $\mu$ sec pulse and a 0.5- $\mu$ sec scanning pulse of equal amplitude.

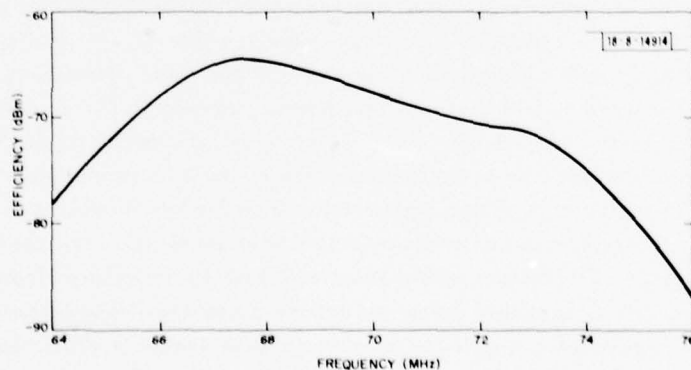
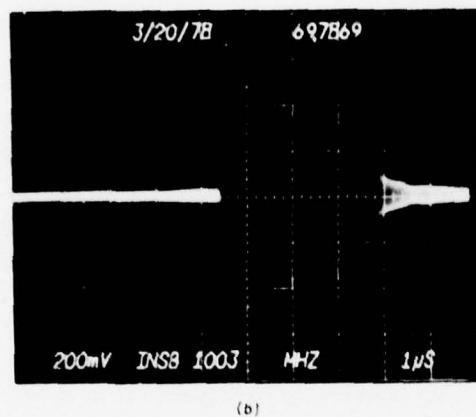


Fig.1-4. Convolution efficiency vs acoustic-wave frequency for InSb/LiNbO<sub>3</sub> convolver at 77 K for a 1300-V bias, and for 4- $\mu$ sec equal-amplitude pulses.

interaction for  $V = 1290$  V is shown in Fig. 1-3(b). To obtain this oscillogram, a 7- $\mu$ sec pulse and a 0.5- $\mu$ sec scanning pulse of equal amplitude were used. The interaction efficiency is constant to  $\leq 1.5$  dB over the device length. A similar uniformity was obtained at flat-band. The linearity of the convolution output was also measured. For a bias of 1200 V, the 1-dB compression point occurred at 18 dBm power input.

The frequency dependence of  $F$  is shown in Fig. 1-4 for a bias of 1300 V. The convolver efficiency seems to follow the transducer bandpass characteristics, and is flat to  $\leq 3$  dB over the range 66 to 70 MHz. These data were taken with a different transducer tuning inductance than was used for the data in Figs. 1-2 and 1-3, so the center frequency for maximum  $F$  is shifted a few megahertz from the earlier figures.

An InSb/LiNbO<sub>3</sub> convolver has been demonstrated at 77 K that has a maximum efficiency comparable to that obtained with Si-diode-array/LiNbO<sub>3</sub> ASIDs. This result suggests the possibility of using a high-density InSb-diode-array/LiNbO<sub>3</sub> structure as a solid state infrared imaging device.

F.J. Leonberger    S.A. Reible  
R.W. Ralston       F.J. O'Donnell

## B. OPTICALLY PUMPED HgCdTe LASERS

For the first time, CW laser operation has been achieved with Hg<sub>1-x</sub>Cd<sub>x</sub>Te. Liquid-phase epitaxially grown HgCdTe crystals, which were cooled to approximately 12 K and optically pumped with a Nd:YAG laser, were found to lase continuously at 2.79  $\mu$ m. In addition, pulsed stimulated emission in various HgCdTe crystals was observed at 77 K in the wavelength range from 1.25 to 2.97  $\mu$ m using a Q-switched Nd:YAG laser. Previously, pulsed HgCdTe lasers<sup>7</sup> at 12 K emitting at 3.7 and 4.1  $\mu$ m were reported for Bridgman-grown HgCdTe optically pumped with a GaAs diode laser. Also, pulsed stimulated spin-flip Raman scattering emission from Hg<sub>0.766</sub>Cd<sub>0.234</sub>Te at 12 K using a CO<sub>2</sub> laser pump was observed.<sup>8</sup> Pulsed laser action at 10 to 15 K has been reported at 0.78  $\mu$ m in CdTe excited by electron-beam pumping.<sup>9</sup>

The HgCdTe crystals were films, which were grown by a liquid-phase epitaxial technique onto CdTeSe substrates. The LPE growth was carried out using a Te solution at 450°C, which was saturated with a CdTe source seed prior to growth. The cooling rate and growth time were 8°C/min. and 52 sec, respectively. The melt equilibration time and temperature were 48 min. and 535°C, respectively. The Bridgman-grown CdTeSe substrates were oriented (111)B and etched in a 10-percent Br-CH<sub>3</sub>OH solution for 10 to 15 sec just prior to loading into the modified horizontal open-tube slider-type LPE apparatus. Figure 1-5(a) shows an optical photomicrograph of a (110)-cleaved cross section of a 3- $\mu$ m-thick Hg<sub>0.557</sub>Cd<sub>0.443</sub>Te layer grown on a CdTe<sub>0.959</sub>Se<sub>0.041</sub> substrate, and Fig. 1-5(b) shows the as-grown surface of the same wafer. A pattern of three sets of intersecting lines is clearly seen in Fig. 1-5(b). The depth of the surface structure is not resolved in Fig. 1-5(a) and is estimated to be  $< 1000$  Å. This surface morphology is typical of good-quality single-crystal films grown on (111) substrates. As-grown samples with lateral dimensions of about 4 × 12 mm were cleaved into small rectangular parallelepipeds with typical dimensions of 0.15 × 0.2 × 2 mm and mounted with thermal compound grease onto a copper heat sink. The HgCdTe films were p-type with  $\sim 10^{16}$  carriers/cm<sup>3</sup> at 77 K. The samples were optically pumped on the as-grown (111) faces, with the laser cavity formed by the two cleaved (110) end faces. The incident 1.06- $\mu$ m laser pump beam was focused onto the HgCdTe film to a rectangular pattern using crossed cylindrical BaF<sub>2</sub> lenses with a

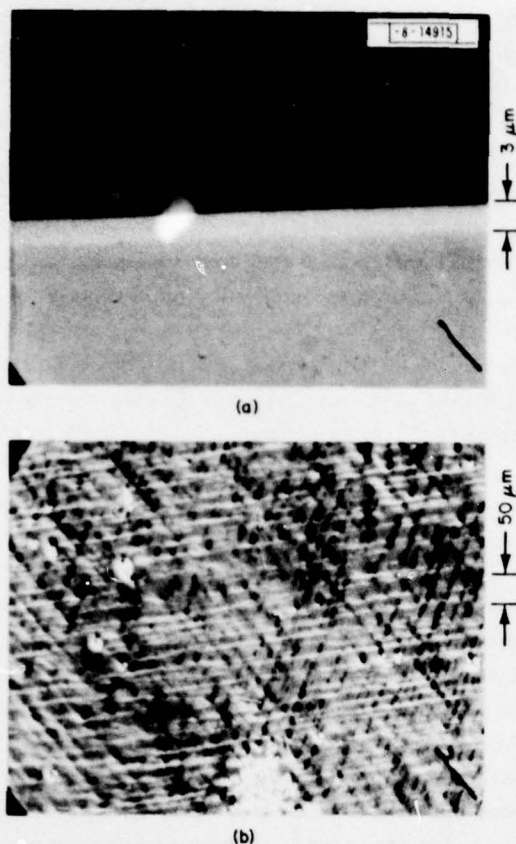


Fig. I-5. (a) Optical photomicrograph of (110) cleaved section of a crystal prepared by LPE on a (111)B CdTeSe substrate. (b) As-grown surface of a LPE growth of  $\text{Hg}_{0.557}\text{Cd}_{0.443}\text{Te}$  on a (111)B  $\text{CdTe}_{0.959}\text{Se}_{0.041}$  substrate.

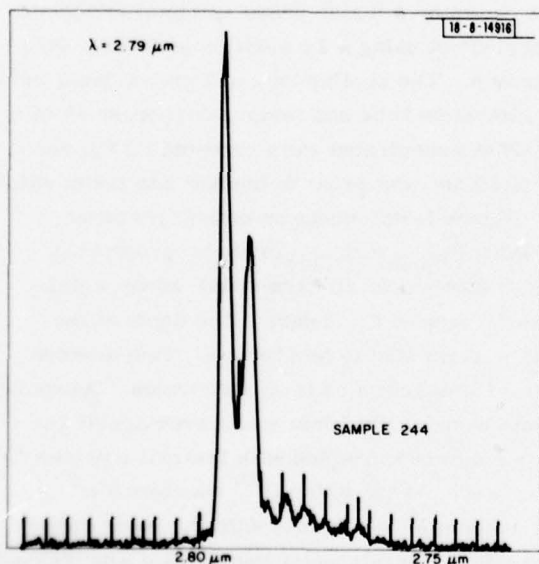


Fig. I-6. CW emission spectrum of a  $\text{Hg}_{0.557}\text{Cd}_{0.443}\text{Te}$  LPE grown layer optically pumped with a Nd:YAG laser.

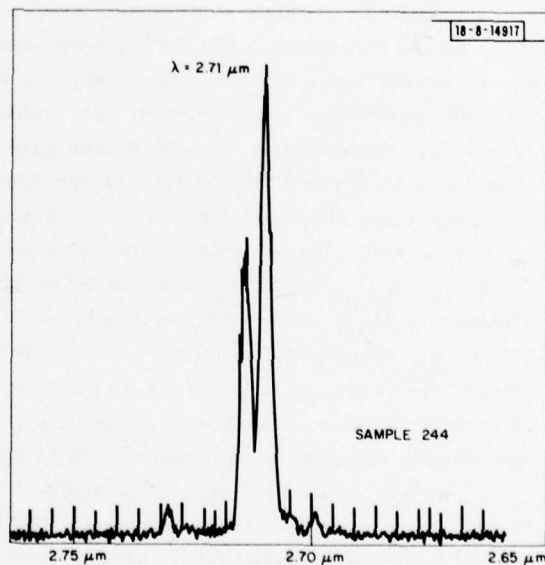


Fig. I-7. Pulsed emission spectrum of a  $\text{Hg}_{0.557}\text{Cd}_{0.443}\text{Te}$  LPE grown layer optically pumped with a Nd:YAG laser.



stripe width of 25  $\mu\text{m}$  and a length which corresponded to the distance between the cleaved faces. The CW radiation from the HgCdTe was mechanically chopped for phase-sensitive detection, passed through a grating spectrometer, a Ge filter, and detected by a PbS detector cooled to 198 K.

Continuous-wave operation at 2.79  $\mu\text{m}$  was observed at approximately 12 K for the sample shown in Fig. I-5(a-b). Figure I-6 illustrates the mode structure for the sample, which was optically pumped about 1.5 times threshold ( $\sim 1.5$  mW of Nd:YAG laser power absorbed by the film). The small number of modes shown in Fig. I-6 is typical of the spectra of these samples. If the entire volume ( $25 \times 210 \times 3 \mu\text{m}^3$ ) of HgCdTe is lasing uniformly, then the laser threshold is remarkably low, i.e.,  $< 20 \text{ W/cm}^2$  (equivalent to a diode-laser injected current density of  $< 16 \text{ A/cm}^2$ ). The equivalent threshold injection current densities are considerably lower than those observed in optically pumped InSb (Ref. 10). The absolute (not differential) external quantum efficiency (assuming equal power out of both ends of the laser) was estimated to be approximately 5 percent after taking into account reflection losses from the HgCdTe surface (28 percent), losses in the KRS-5 output optics window (25 percent), and absorption-reflection losses in the Ge output optics filter (47 percent). For a typical input power absorbed by the HgCdTe of 1.5 mW, the total output power emitted was estimated to be approximately 75  $\mu\text{W}$ .

The emission spectrum of a  $\text{Hg}_{0.557}\text{Cd}_{0.443}\text{Te}$  LPE grown layer optically pumped with a Q-switched Nd:YAG laser at 77 K is shown in Fig. I-7. The 3- $\mu\text{m}$ -thick film of HgCdTe on a CdTeSe substrate shown in Fig. I-5(a-b) was excited by 250-msec pulses (repetition rate of 4.7 kHz) from a Q-switched Nd:YAG laser. The average and peak laser powers absorbed by the film were approximately 1.5 mW and 1.3 W, respectively. The power density threshold for lasing at 77 K is  $< 17 \text{ kW/cm}^2$ , and the measured HgCdTe emission wavelength is 2.71  $\mu\text{m}$ . From the wavelength separation of adjacent longitudinal modes, the equivalent index of refraction (i.e.,  $\bar{n} = \lambda^2 / 2L\Delta\lambda$ , where  $\lambda$  is the lasing wavelength,  $L$  is the cavity length, and  $\Delta\lambda$  is the longitudinal mode spacing) is  $\bar{n} = 3.6$ .

Table I-1 summarizes the results of optically pumping several LPE grown films of  $\text{Hg}_{1-x}\text{Cd}_x\text{Te}$  with a Q-switched Nd:YAG laser. The HgCdTe laser emission wavelengths varied from 1.25 to 2.97  $\mu\text{m}$  as the CdTe content of the films varied from 0.729 to 0.410, respectively.

TABLE I-1 LASER EMISSION WAVELENGTH AT 77 K VS MOLE-FRACTION CdTe FOR SEVERAL $\text{Hg}_{1-x}\text{Cd}_x\text{Te}$ LPE GROWN FILMS			
Sample No.	Laser Emission Wavelength ( $\mu\text{m}$ )	Mole-Fraction CdTe (x)	Film Thickness ( $\mu\text{m}$ )
160	1.25	$0.729 \pm 0.005$	4
244	2.71	$0.443 \pm 0.006$	3
255	2.58	$0.454 \pm 0.007$	10
256	1.66	$0.596 \pm 0.005$	7
257	2.97	$0.410 \pm 0.004$	6

The HgCdTe compositions were determined from electron microprobe measurements. Various film thicknesses have been used between 3 and 10  $\mu\text{m}$ . The laser emission energies vs mole fraction of CdTe at 77 K are slightly lower than the energy-gap values calculated from an empirical expression (Eq. 3) of Scott.<sup>11</sup>

Although numerous attempts to obtain laser action in HgCdTe by optical pumping have been made in the past, success was achieved in only two samples.<sup>7</sup> In our present experiments, the unique low-temperature LPE growth (i.e., 450°C) from Te solution may yield a material with a reduced density of nonradiative centers, so that the ratio of radiative to nonradiative transitions is enhanced and laser action occurs easily. We plan to investigate longer-wavelength devices in the near future. Due to the high-electrooptic figure of merit, lattice-matching capability, low laser threshold, spectral range from 0.85  $\mu\text{m}$  to the far-infrared, and LPE technology, HgCdTe has considerable potential for integrated optical circuit applications as well as for various component devices, such as diode lasers, waveguides, detectors, modulators, solar cells, etc.

T. C. Harman  
M. C. Finn

#### REFERENCES

1. Solid State Research Report, Lincoln Laboratory, M.I.T. (1978:1), pp. 5-10.
2. C. E. Hurwitz and J. P. Donnelly, *Solid-State Electron.* **18**, 753 (1975), DDC AD-A016705/6.
3. J. P. Donnelly and C. E. Hurwitz, *Appl. Phys. Lett.* **31**, 418 (1977), DDC AD-A050856.
4. S. A. Reible, J. H. Cafarella, R. W. Ralston, and E. Stern, in 1976 Ultrasonics Symposium Proceedings (IEEE, New York, 1976), p. 451, DDC AD-A040519/1.
5. Solid State Research Report, Lincoln Laboratory, M.I.T. (1977:4), p. 53, DDC AD-A052463.
6. H. Gautier and G. S. Kino, *IEEE Trans. Sonics Ultrason.* **SU-24**, 23 (1977).
7. I. Melngailis and A. J. Strauss, *Appl. Phys. Lett.* **8**, 179 (1966), DDC AD-642208.
8. J. P. Sattler, B. A. Weber, and J. Nemarick, *Appl. Phys. Lett.* **25**, 491 (1974); B. A. Weber, J. P. Sattler, and J. Nemarick, *Appl. Phys. Lett.* **27**, 93 (1975).
9. V. S. Vavilov and E. L. Nolle, *Dokl. Akad. Nauk SSSR* **164**, 73 (1965).
10. A. S. Pine and N. Menyuk, *Appl. Phys. Lett.* **26**, 231 (1975).
11. M. W. Scott, *J. Appl. Phys.* **40**, 4077 (1969).

## II. QUANTUM ELECTRONICS

### A. HAND-HELD $\text{NdP}_5\text{O}_{14}$ LASER

In order to demonstrate the miniaturization possible with high-Nd-concentration lasers, we have constructed a self-contained, hand-held laser using a flash-lamp-excited  $\text{NdP}_5\text{O}_{14}$  (NPP) rod. For increased ruggedness and miniaturization, we have replaced the hollow pump collector assembly of our previous NPP laser head<sup>1</sup> by a solid integral assembly. This consists of a 1-cm-long  $\times$  6-mm-diam sapphire cylinder, with a round hole to accommodate the 2.5-mm-diam Xe flash lamp and a 1-mm-square slot to hold the NPP laser rod, both of which are mounted using polystyrene cement. The outer surfaces of the sapphire collector were aluminized and overcoated with silicon oxide for protection. These components are shown in Fig. II-1.

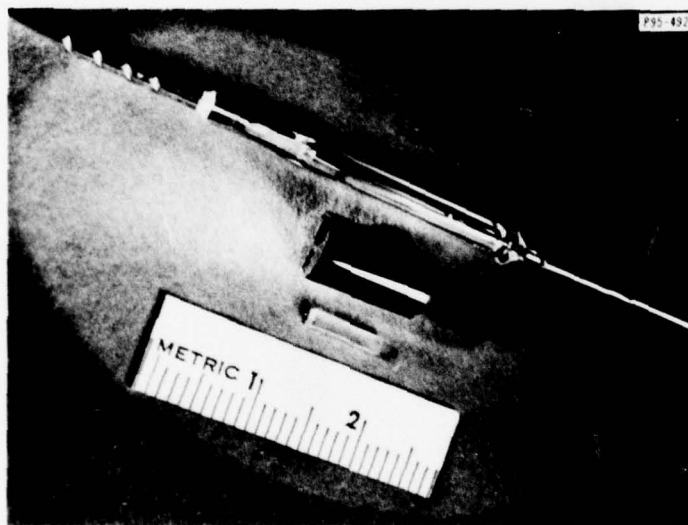


Fig. II-1. Laser head components, showing (from top to bottom) Xe flash lamp, sapphire pump collector, and NPP rod.

The laser head was mounted in a Vespel holder to which were attached the 1/2-in.-diam laser mirrors, using adjustable O-ring mounts. The present laser has a semi-confocal cavity with a 13-cm-radius high-reflecting mirror and a flat, 10-percent transmitting output mirror.

The laser-cavity assembly is mounted on top of a power supply (2-1/2  $\times$  3  $\times$  5-3/4 in.) containing a commercially purchased DC inverter with LC pulse-forming network and SCR trigger circuitry. The inverter is powered by rechargeable 12-V Ni-Cd batteries, also mounted in the power supply, capable of providing one thousand 1-J discharges into the lamp. The laser is fired manually by a push-button switch at rates up to 1 Hz. The complete laser is shown in Fig. II-2.

The laser rod presently in use is 1/2  $\times$  1  $\times$  7 mm. The internal lamp and rod-mounting surfaces on the sapphire collector have a ground finish, which we have not index-matched to the lamp and rod. Because of these factors, we are presently limited to 0.5 mJ output at 1.05  $\mu\text{m}$ .



Fig. II-2. Complete NPP laser, with cylindrical laser cavity mounted on top of power supply.

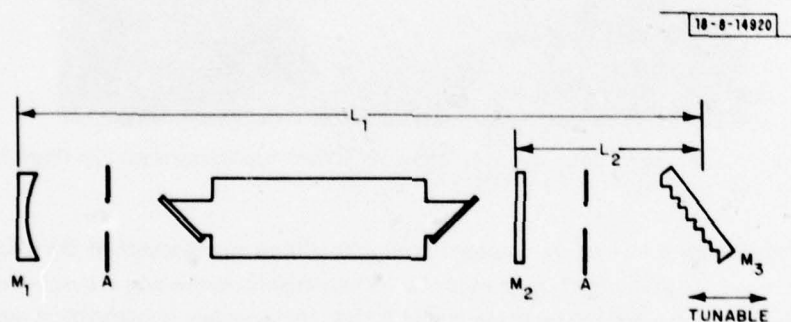


Fig. II-3. Experimental arrangement of line-tunable laser. A - apertures;  $M_1$  - curved ZnSe mirror, 1-m radius, 85-percent reflectivity;  $M_2$  - planar ZnSe mirror, 63-percent reflectivity;  $M_3$  - tunable grating;  $L_1 = 62$  cm,  $L_2 = 17$  cm.



Using a 1-mm<sup>2</sup> rod and better cementing techniques, we should be able to achieve output energies comparable to the 8-mJ level (at 1-J input) obtained with our laboratory-bench hollow-collector laser heads.

The size of the present resonator assembly is determined primarily by the external mirrors and mounts. Using miniature mirrors fastened directly to the sapphire holder, or suitably polishing and coating the laser-rod surfaces themselves, would result in a much smaller laser assembly. Significant reduction in the power-supply size should also be achievable.

S. R. Chinn  
W. E. Barch  
W. K. Zwicker†

## B. MINI-TEA LASER

As described in previous reports,<sup>2,3</sup> we have designed and operated a mini-TEA CO<sub>2</sub> laser which has a volume energy extraction comparable to larger, conventional CO<sub>2</sub> TEA lasers. In our recent work, we have operated the mini-TEA laser with a "three-mirror" grating-tuned cavity. We have also obtained up to 3.6 W of average power output and operated at a pulse repetition frequency (PRF) of up to 250 Hz.

The loss in laser efficiency when one of the laser mirrors is replaced by a grating can be reduced by use of a three-mirror cavity.<sup>4,5</sup> Such cavities are constructed, in grating-tuned cavities, by placing a partially reflecting mirror between the Littrow-mounted grating and active medium to form, with the grating, a tunable reflector with a higher effective reflectivity than that of the grating alone. An additional advantage associated with the three-mirror cavity is the reduction in optical power density at the grating surface, which can prevent optical damage to that surface. We employed such a cavity with the mini-TEA laser; the arrangement is shown in Fig. II-3. The effect of the 63-percent reflector in the system, for a grating reflectivity of 85 to 90 percent, is to increase the effective grating reflectivity to ~98 percent and decrease intensity at the grating by a factor of 8 (see Ref. 4). The laser output in the strongest lines increased by ~20 percent, compared with operation in the conventional cavity without the 63-percent reflector; and optical damage of the grating, which had occurred in the conventional cavity at output energies of 25 mJ, was eliminated. We observed single-line laser output on the P(8) to P(36) and the R(12) to R(28) lines of the (00<sup>0</sup>1) → (10<sup>0</sup>0) transition, and on the P(10) to P(34) and the R(10) to R(26) lines of the (00<sup>0</sup>1) → (02<sup>0</sup>0) transition.

In attempting to increase the PRF of the mini-TEA laser, we noted that changing the gas flow from longitudinal to transverse across the active region increased the maximum PRF from 10 to 40 Hz. Above these values, interelectrode arcing occurred. The latter value was obtained by using holes drilled in the lucite plates on opposite sides of the laser as gas inlets and outlets. The resultant gas flow was inhomogeneous, with a strong possibility of backscatter of discharge products into the active region. Under these conditions, little further improvement was attainable by increasing the gas flow rate.

The side panels of the laser were changed to conical units with rectangular cross sections. This reduced the probability of backscatter from the downstream side of the active region. In addition, a 6-in.-long stilling section with a cross-sectional area comparable to the active area of the laser was placed between the laser and the upstream conical unit.

† Philips Laboratories, Briarcliff Manor, New York.



With this arrangement, PRFs in excess of 200 Hz have been obtained with a clearing ratio of 1.5:1. At this rate the laser generally operates arc-free for the order of 10 to 15 min. Arc-free operation at 250-Hz PRF has been achieved for shorter intervals. Upon going into an arcing mode, it is necessary to significantly decrease the frequency to eliminate the arcing. Once the arcing is stopped, the frequency can quickly be returned to its original value. Average mini-TEA laser power in excess of 3.6 W has been achieved at 200 Hz yielding an energy of 18 mJ/pulse, which compares favorably with the low-PRF value of 25 mJ/pulse produced by the same laser.

The results clearly indicate that the mini-TEA laser is capable of operating at high PRFs with line tunability and at power levels which can be useful for atmospheric optics applications. Having established this, we will completely redesign the gas flow system of the laser.

The present flow system is an open one; that is, the gas flows directly through the laser and into the atmosphere. The case mentioned above of a 200-Hz PRF with a 1.5 clearing ratio corresponds to a gas flow rate of the order of 40 liters/min. For still higher PRF and the higher clearing ratios needed to achieve the highest power levels available, the gas dissipation rate is clearly excessive. For this reason, we will design a semi-open system which will continuously replace a small fraction of a circulating gas flowing at high velocity through the active laser region.

N. Menyuk  
P. F. Moulton

### C. OPTICAL ENERGY EXTRACTION FROM MOLECULAR MERCURY

Detailed measurements have been made of the infrared-laser-initiated extraction of the energy stored in metastable mercury excimers. As described in our previous report,<sup>6</sup> this work is directed toward the development of a scalable, high-power gas laser in the near-ultraviolet for laser fusion applications. Optical pumping from the  $O_g^+$  storage states (see Fig. II-4) to the proposed laser upper state,  $1_u$ , has been extended to higher HF laser powers and to DF and HBr laser pumping. The induced 300 nm emission gave no indication of saturation with infrared-laser power at power densities up to  $\sim 10$  MW/cm<sup>2</sup>. At the highest powers, the laser-induced emission can be more than an order-of-magnitude greater than the thermal value and depends on the temperature, density, and fluorescence wavelength, as will be discussed below.

A careful study has been made of the wavelength dependence of the infrared-induced emission with the experimental configuration shown in Fig. II-5. A grating and a spatial filter, external to the infrared-laser cavity, allow the strongest laser lines to be isolated with a purity of greater than 95 percent. The optically pumped mercury vapor is then probed with the isolated lines. Results for HF and DF lasers are shown in Fig. II-6. The absorption is seen to be remarkably broadband for a bound-bound transition, a fact which may be ascribed to the extremely high density of states in the  $O_g^+$  levels (calculation shows  $\sim 10^4$  cm<sup>-1</sup>). The spectroscopy of such a heavy diatomic molecule may be closely modeled by the methods developed to describe small aromatic hydrocarbons.<sup>7</sup> The apparent resonance in the absorption on the DF P(7),  $2 \rightarrow 1$  line is under closer investigation and is not, at this point, completely understood. However, perturbations between specific  $1_u$  rovibronic levels and those of the nearby levels (see Fig. II-4) will lend oscillator strength to absorption into these specific levels and can produce such resonances. It is important to locate these resonances in order to maximize the extraction efficiency.

The induced ultraviolet emission spectra for HF and DF pumping are shown in Figs. II-7 and II-8. These may be compared with the thermalized emission spectrum, which is also shown.



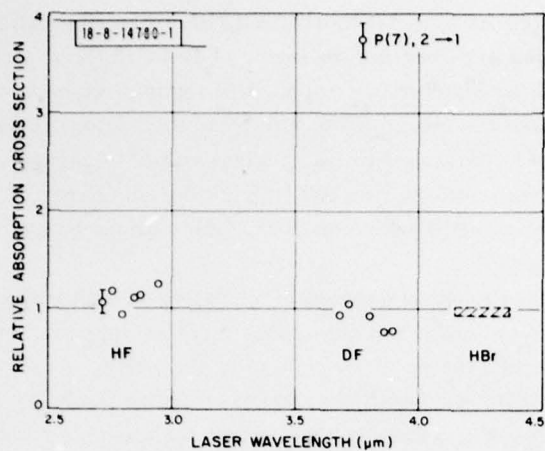


Fig. II-6. Absorption coefficient vs infrared-laser wavelength.

Fig. II-7. HF induced spectrum.

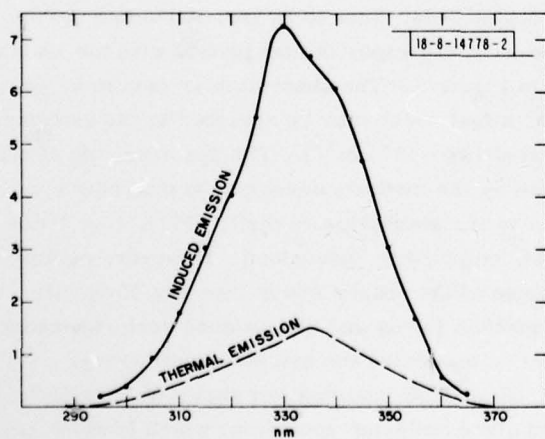
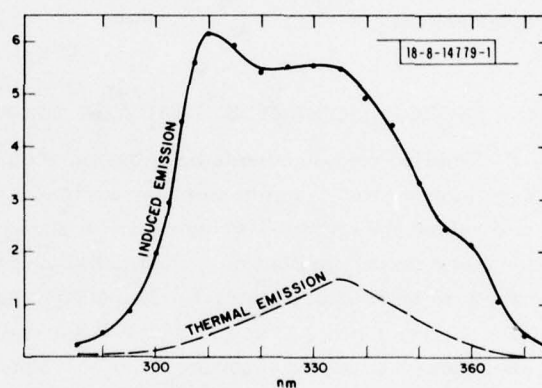


Fig. II-8. DF induced spectrum.



It is clear that, even at densities of  $10^{19} \text{ cm}^{-3}$ , the emission is, to a large extent, unrelaxed fluorescence from the laser-excited states. Making use of the analysis of Smith *et al.*,<sup>8</sup> it is possible to assign the energies of the states being accessed by the infrared laser and, therefore, to determine the variation of the Franck-Condon overlap for the various transitions pumped. This procedure shows that the Franck-Condon factors for the  $O_g^\pm$  to  $1_u$  transition are very nearly constant for both HF and DF wavelengths over a range of several thousand  $\text{cm}^{-1}$ .

The temperature and density dependencies of the induced emission have been studied over ranges of  $300^\circ$  to  $550^\circ\text{C}$  and  $10^{18}$  to  $10^{19} \text{ cm}^{-3}$ , respectively. There is no significant temperature dependence, in agreement with the nearly constant Franck-Condon overlap which has been discussed. The density dependence is also slow, showing quenching with a bimolecular rate constant of  $\sim 2 \times 10^{-13} \text{ cm}^3/\text{sec}$ . This second result is surprising since values more than two orders of magnitude larger have been measured by Stock *et al.*,<sup>9</sup> for similar relaxation processes in this system. However, the experimental approach of Stock *et al.* was significantly different from ours, since their excitation was via high vibronic levels of the  $1_u$  state. In this case, it is possible that different ensembles of vibronic levels would be involved in the two experiments. The dissociation of high-lying  $1_u$  levels is known to be rapid; thus, the rates measured in the two experiments would not be the same. An effort is now being made to resolve this question by extending these measurements to lower densities. This will involve the use of an ArF laser to prepare larger excimer populations at lower atomic densities. Knowledge of the bimolecular quenching rate is important in order to specify the maximum Hg pressure of the laser.

D. J. Ehrlich  
R. M. Osgood, Jr.

#### D. GENERATION OF TUNABLE FAR-INFRARED RADIATION

Concurrent with the heterodyne detector effort in the far-infrared/submillimeter region, we are seeking sources of tunable radiation for applications to spectroscopy, to frequency standards, and to remote sensing. The GaAs Schottky-diode mixer (see p. 35 in Ref. 6) which we have developed for our sensitive receiver and radiometer can be used as a source of tunable laser-sideband radiation and high-order microwave harmonics. Since the corner-reflector configuration acts as an efficient receiver of radiation, it will act reciprocally as an efficient radiator. The resistive nonlinearity of the diode provides the mixing and harmonic-generation mechanism.

In our initial experiments, radiated sidebands of a  $\text{CH}_3\text{I}$  submillimeter laser line at  $447 \mu\text{m}$  were generated and detected using two corner-reflector diode mixers. One diode mixer was simultaneously illuminated by the far-infrared laser and fed coaxially by microwave sources ranging from 2.5 to 18 GHz. A second diode mixer was then used as a high-sensitivity heterodyne receiver to detect the radiated sidebands of the laser signal. Signals of about  $10^{-7} \text{ W}$ , continuously tunable over  $0.5 \text{ cm}^{-1}$ , were observed. Extending this approach further, we investigated the use of these diode mixers as high-order harmonic-signal sources. The experimental arrangement is shown in Fig. II-9, with the microwave radiation between 17 and 37 GHz introduced via the IF connector line to the diode. Radiation generated as high as the 40th harmonic was then detected by a second diode mixer in our standard heterodyne-receiver configuration. In one particular case, a 37-GHz GaAs Gunn oscillator was used to generate 761 GHz. This solid state source coupled with the rugged harmonic mixer provided a compact, stable,

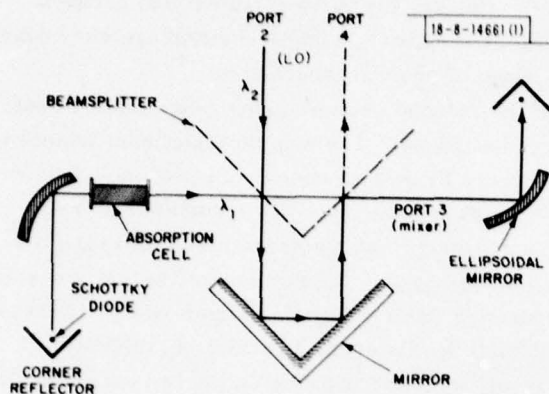
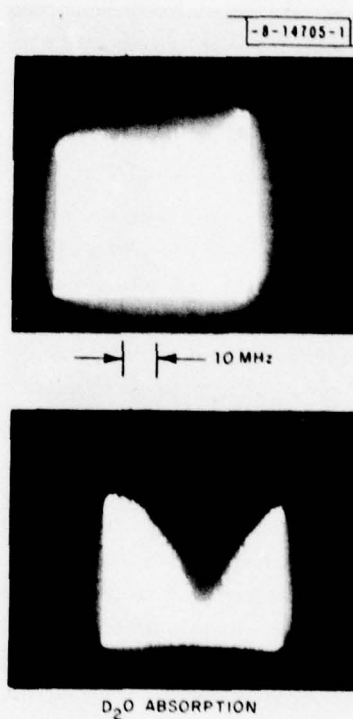


Fig. II-9. Experimental high-resolution spectrometer using quasi-optical diplexer and two Schottky-diode mixers.

Fig. II-10. Photographs of spectrum analyzer at 3 GHz showing transmission of an absorption cell with (below) and without (above) D<sub>2</sub>O gas. Design resolution of this system is 10 kHz ( $3 \times 10^{-7} \text{ cm}^{-1}$ ) with continuous tunability  $\approx 1 \text{ cm}^{-1}$ .



tunable source of about  $5 \times 10^{-11}$  W in the submillimeter. Because of the sensitivity of our heterodyne receiver, the observed S/N exceeded 35 dB on a spectrum analyzer having a 100-kHz bandwidth.

High-resolution far-infrared spectroscopic studies using both these source-detector systems are now under way. As a first demonstration, an absorption cell containing  $D_2O$  gas at low pressure was placed in one arm of the spectrometer (as shown in Fig. II-9), 35.7-GHz radiation from a microwave source was used to drive the mixer diode, and the 17th harmonic generated (607.345 GHz), after passing through the absorption cell, was detected by the heterodyne receiver. The LO was supplied by an optically pumped  $CH_3F$  laser operating at 604.295 GHz, giving an IF around 3 GHz. Tuning through the  $D_2O$  absorption line was accomplished by tuning the microwave source. Figure II-10 shows the far-infrared output with and without the gas. Because of residual pressure from condensed liquid in the absorption cell, the linewidth could not be reduced below the 20 MHz shown. The resolution of the spectrometer is about 100 kHz, being presently limited by the stability of the laser LO.

This preliminary work will now be continued with other gases that have absorptions near strong laser LO lines, and will be applied particularly to atomic fine structure resonance lines that have extremely narrow and stable transitions which can be used as references for far-infrared frequency standards.

H. R. Fetterman      B. J. Clifton  
W. A. M. Blumberg    C. D. Parker  
P. E. Tannenwald

#### E. INFRARED ABSORPTION STUDIES OF $CO_2$ -LASER-EXCITED $SF_6$

We have extended the infrared-infrared double-resonance measurements of  $SF_6$  previously reported (see Ref. 10 and p. 21 in Ref. 3) to  $CO_2$ -laser fluences as high as  $1 \text{ J/cm}^2$ . A paper based on these results is currently being prepared for publication; only a brief summary of the conclusions is presented here.

- (1) The absorption spectrum immediately following the  $CO_2$ -laser pulse shows a strong red shift.
- (2) The spectrum shows a pronounced shift of absorption strength toward higher frequency on a time scale of several microseconds. This shift is independent of excitation level over the 3- to 10-photons/molecule range.
- (3) This variation in the absorption spectrum is most plausibly interpreted as a "cooling" of the  $\nu_3$  vibrational mode and a redistribution of the internal vibrational energy among the remaining vibrational degrees of freedom.
- (4) At the 3-photons/molecule excitation level, the observed spectra are similar to shock-tube measurements of the  $\nu_3$ -mode absorption spectra of hot  $SF_6$ , and the measured spectra are in reasonable agreement with the thermal spectrum expected at this fluence for complete vibrational energy thermalization.
- (5) At the 10-photons/molecule excitation level, the observed spectra are no longer as well described by a thermal distribution.

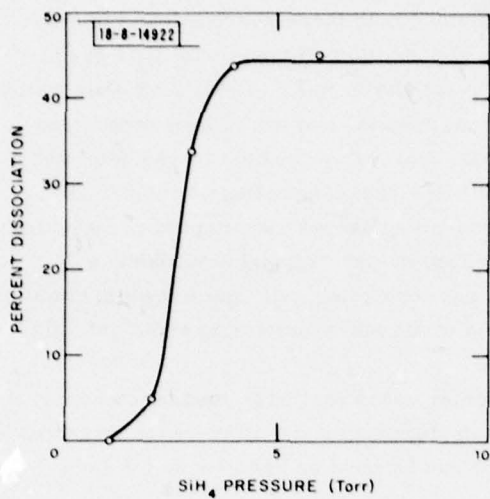
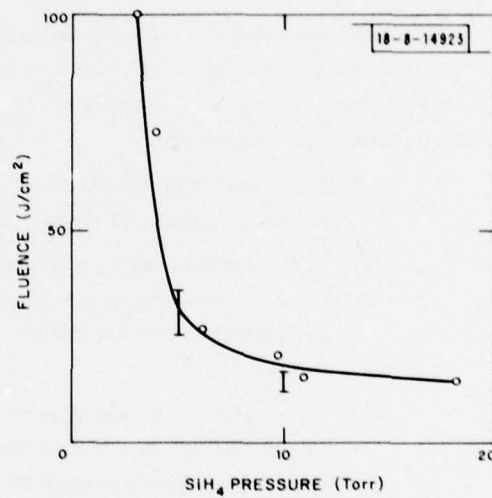


Fig. II-11. Pressure dependence of dissociation of SiH<sub>4</sub> at a fluence of 140 J/cm<sup>2</sup> at 944.2 cm<sup>-1</sup>, P(20) line.

Fig. II-12. Fluence at luminescence threshold vs silane pressure, P(20) pump.





- (6) Although some collisions do occur and are indeed required for our measurement, we have not observed any pressure dependence of this spectral relaxation; this suggests that it may reflect a collisionless intramolecular energy randomization.
- (7) A much broader induced absorption band, approximately two orders of magnitude weaker than the "hot"  $\nu_3$  absorption spectrum, has been observed on the high-frequency side of the  $\nu_3$  band. This spectrum extends more than  $100\text{ cm}^{-1}$  above  $\nu_3$  and is in qualitative agreement with the multiphoton excitation spectrum found in two-frequency dissociation experiments. This is the first direct observation of the blue quasi-continuum.

T. F. Deutsch  
S. R. J. Brueck

#### F. $\text{CO}_2$ -LASER-INDUCED DISSOCIATION OF $\text{SiH}_4$

The infrared-laser-induced photochemistry of silane is of interest from several standpoints. While it was established in the early experiments of Basov *et al.*<sup>11</sup> that a CW  $\text{CO}_2$  laser can dissociate  $\text{SiH}_4$  at pressures of 200 Torr into silicon and hydrogen, it has not been determined if  $\text{SiH}_4$  can undergo collisionless multiphoton dissociation in the same fashion as  $\text{SF}_6$ ,  $\text{BCl}_3$ , and a number of other molecules. Silane-based reactions may have application to visible lasers; for example,  $\text{CO}_2$ -laser-induced decomposition of silane has been suggested as a possible source of Si atoms to generate visible laser action in SiO using the oxidation of silicon,<sup>12</sup> and the laser-initiated reaction of  $\text{SiH}_4$  with  $\text{SF}_6$  has recently been used to obtain visible luminescence from  $\text{S}_2$  (see Ref. 13).

We have studied the  $\text{CO}_2$ -laser-induced chemistry of silane in order to characterize the energy absorption, visible luminescence, and dissociation processes involved. A publication describing the experiments in detail is in preparation; the main results are summarized here. Studies of energy deposition in  $\text{SiH}_4$  by a  $\text{CO}_2$  TEA laser using both optoacoustic<sup>14</sup> and direct transmission measurements showed that the absorption is only 1.5 photons/molecule at a fluence of  $0.8\text{ J/cm}^2$ , 1-Torr  $\text{SiH}_4$ , and 180-nsec-wide P(20)  $\text{CO}_2$  pulses. By contrast,  $\text{SF}_6$  at this same fluence absorbs  $\sim 7$  photons/molecule in a collisionless regime. The pressure dependence of the dissociation of  $\text{SiH}_4$  at a fluence of  $140\text{ J/cm}^2$  at  $944.2\text{ cm}^{-1}$ , P(20) line is presented in Fig. II-11 and shows that dissociation is a collisional process. Figure II-12 shows the fluence at the threshold for visible luminescence, which correlates well with the behavior of the dissociation. The luminescence is accompanied by electrical conductivity; the spectral content of the radiation has been examined using an optical multichannel analyzer. The spectrum consists mainly of molecular and atomic hydrogen lines, although a few lines remain unidentified. The difference between the behavior of  $\text{SF}_6$  and  $\text{SiH}_4$  under  $\text{CO}_2$ -laser excitation is attributed to the fact that the density of states in the latter is sufficiently low to make collisionless multiphoton dissociation impossible.

T. F. Deutsch

# REFERENCES

1. S. R. Chinn and W. K. Zwicker, Appl. Phys. Lett. 31, 178 (1977).
2. Solid State Research Report, Lincoln Laboratory, M.I.T. (1977:3), p. 17, DDC AD-A050551.
3. Ibid. (1977:4), p. 18, DDC AD-A052463.
4. J. E. Bjorkholm, T. C. Damen, and J. Shah, Opt. Commun. 4, 283 (1971).
5. G. J. Ernst and W. J. Witteman, IEEE J. Quantum Electron. QE-7, 484 (1971).
6. Solid State Research Report, Lincoln Laboratory, M.I.T. (1978:1), p. 32.
7. G. W. Robinson, J. Chem. Phys. 47, 1967 (1967).
8. E. W. Smith, R. E. Drullinger, M. M. Hessel, and J. Cooper, J. Chem. Phys. 66, 5667 (1977).
9. M. Stock, E. W. Smith, R. E. Drullinger, and M. M. Hessel (private communication).
10. T. F. Deutsch and S. R. J. Brueck, Chem. Phys. Lett. 54, 258 (1978).
11. N. G. Basov, E. P. Markin, A. N. Oraevskii, A. V. Pankratov, and A. N. Skachkov, JETP Lett. 14, 165 (1971).
12. A. S. Bashkin, N. L. Kupriyanov, and A. N. Oraevskii, Sov. J. Quantum Electron. 7, 595 (1977).
13. S. H. Bauer and J. A. Haberman, IEEE J. Quantum Electron. QE-14, 233 (1978).
14. T. F. Deutsch, Opt. Lett. 1, 25 (1977).

### III. MATERIALS RESEARCH

#### A. ELECTRICAL PROPERTIES OF InP

Infrared diode lasers<sup>1</sup> and avalanche photodiodes<sup>2</sup> utilizing GaInAsP epitaxial layers grown on InP substrates are promising sources and detectors for fiber optics communications at 1.1 to 1.3  $\mu\text{m}$ . In order to provide InP substrate material for these devices, we have been synthesizing polycrystalline InP from the elements and then growing single crystals of the compound by the liquid-encapsulated Czochralski (LEC) method.<sup>3</sup> In this report, we summarize the results of resistivity ( $\rho$ ) and Hall coefficient ( $R_H$ ) measurements made on the polycrystalline material and on numerous n-type, semi-insulating, and p-type LEC crystals.

Polycrystalline InP is synthesized from the elements inside an evacuated, sealed, fused-silica ampoule in a horizontal two-zone furnace.<sup>4</sup> The In is placed in a fused-silica boat at one end of the ampoule, and the P is placed at the other end. The In boat is heated to  $\sim 1000^\circ\text{C}$ , and the P reservoir is heated to a constant temperature in the  $420^\circ$  to  $480^\circ\text{C}$  range. A molten In-P solution is formed in the boat by transfer of P vapor from the reservoir, then solidified directionally to form an InP ingot. In early runs, solidification was accomplished by gradually lowering the temperature of the hot zone, but now is achieved by pulling the ampoule toward the cold end of the furnace. Solidification rates between 1 and 5 cm/day have been used.

Only a minority of the polycrystalline ingots have yielded samples suitable for electrical measurements, since the grain size in most of the ingots has been too small. All samples that have been measured are n-type. For these samples the electron mobilities ( $\mu = R_H/\rho$ ) at 77 and 300 K are plotted in Fig. III-1 vs the electron concentration ( $n = -1/R_H e$ ) at 300 K. Due to ionized impurity scattering,  $\mu_{77}$  generally decreases with increasing  $n_{300}$ , which is approximately equal to  $n_{77}$ . The samples with  $n_{300}$  above  $10^{16} \text{ cm}^{-3}$  were obtained from ingots prepared early in the program, before satisfactory techniques were developed for handling the elements and sealing the synthesis ampoules. The latest ingot, which used In from Johnson Matthey and P from Mining and Chemical Products, was solidified at a rate of about 2.5 cm/day with a P reservoir temperature of  $425^\circ\text{C}$ . For a sample from the center of this ingot,  $n = 1.5 \times 10^{15} \text{ cm}^{-3}$  and  $\mu_{77} = 6.0 \times 10^4 \text{ cm}^2 \text{ V}^{-1} \text{ sec}^{-1}$ , indicating that there is very little acceptor compensation. These values approach the best so far reported for polycrystalline InP (Ref. 4). Additional work is in progress to determine the best sources of In and P, to improve the cleanliness of the handling procedures, and to check the effect of different boat materials such as BN and vitreous carbon on InP purity.

The LEC technique is the best method now available for growing bulk single crystals of InP, but several problems remain. Unless the growth conditions are maintained within fairly narrow limits, the yield of single-crystal boules is very low because of twinning and subsequent nucleation of new grains at the intersections of twin planes. In addition, constitutional supercooling is often troublesome because the polycrystalline charge usually contains metallic In inclusions and is therefore nonstoichiometric. We believe that a large temperature gradient at the crystal-melt interface minimizes both effects. If the gradient in the growing crystal becomes too large, however, the defect density is expected to increase due to strain. We have not made temperature-gradient measurements in our LEC crystal puller, which uses an rf induction generator to heat a graphite susceptor containing the melt crucible, but we have varied the gradient by raising or



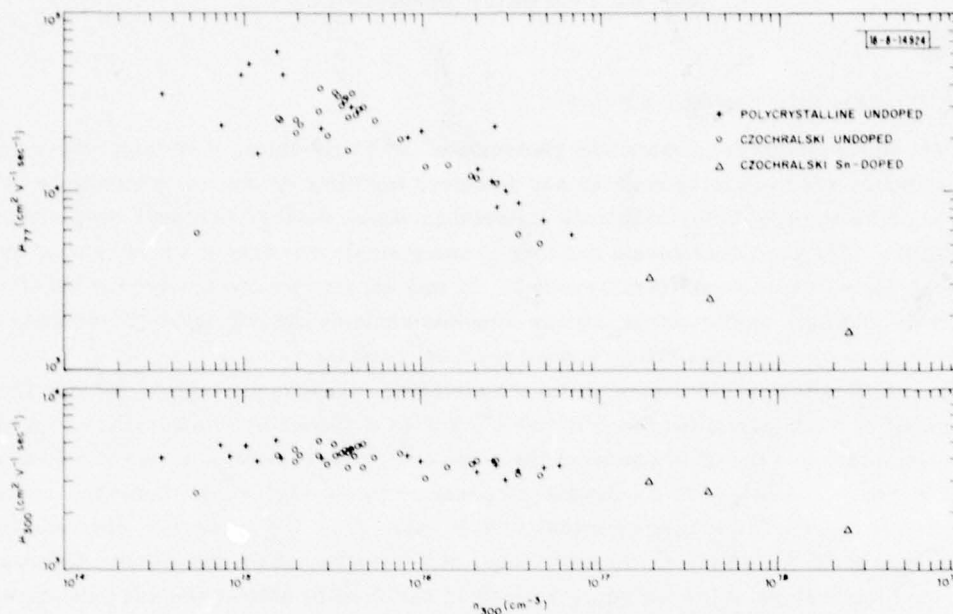


Fig. III-1. Electron mobilities at 77 and 300 K ( $\mu_{77}$  and  $\mu_{300}$ ) as a function of electron concentration at 300 K ( $n_{300}$ ) for n-type samples of InP from undoped polycrystalline ingots and from undoped or Sn-doped boules grown by LEC technique.

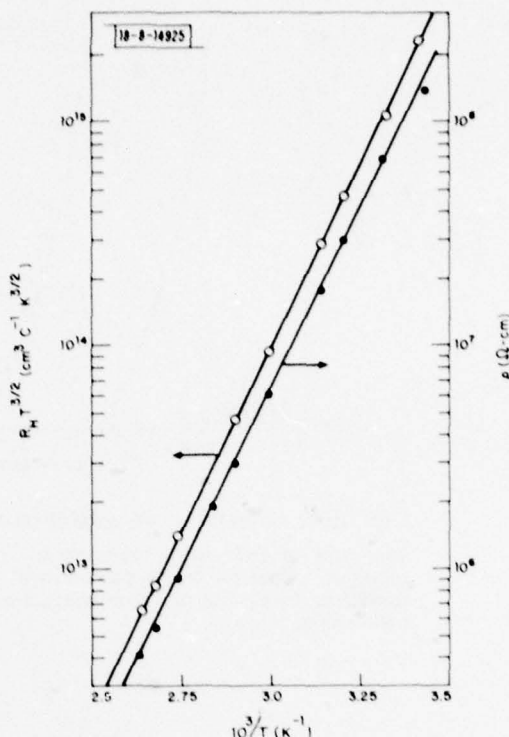
lowering the susceptor with respect to the rf coil. In recent runs we have employed a BN crucible 5 cm in diameter and 5 cm high, an InP charge of 160 g, a pre-baked  $B_2O_3$  encapsulant charge of 30 g, a square InP seed with the (111)P face down, Ar gas pressures of 40 to 45 atm, and pull rates of 1 to 2.5 cm/hr. Over half the boules grown under these conditions consist mainly of a single crystal.

All samples from nominally undoped LEC boules have been n-type. The  $n$  and  $\mu$  data for these samples and for samples from three Sn-doped boules ( $n > 10^{17} \text{ cm}^{-3}$ ) are included in Fig. III-1. Where electrical measurements were made on samples from the polycrystalline charge used for growth of an undoped boule, the data for the charge and boule have been compared in order to estimate the amount of contamination resulting from the LEC growth process. In the worst case, the total ionized impurity concentration (as estimated from  $n_{77}$  and  $\mu_{77}$ ) increased by less than  $\sim 5 \times 10^{15} \text{ cm}^{-3}$ , while two boules contained  $\sim 1 \times 10^{15} \text{ cm}^{-3}$  fewer ionized impurities than their charges. The highest value of  $\mu_{77}$  that we have measured to date for LEC InP is  $3.8 \times 10^4 \text{ cm}^2 \text{ V}^{-1} \text{ sec}^{-1}$ , for a sample with  $n_{300} = 2.7 \times 10^{15} \text{ cm}^{-3}$ .

To obtain semi-insulating InP, we have used the technique of doping with Fe, a deep acceptor with an energy level located near the center of the InP bandgap.<sup>5</sup> Elemental Fe is loaded into the BN crucible along with the polycrystalline charge, and LEC growth is carried out under conditions similar to those described above. To determine the activation energy for thermally excited electrons from the Fe acceptor level to the conduction band,  $R_H$  and  $\rho$  were measured over the temperature range from 290 to 380 K for a semi-insulating sample from an Fe-doped boule. For this sample,  $n_{300} = 2.3 \times 10^7 \text{ cm}^{-3}$ ,  $\rho_{300} = 7.6 \times 10^7 \Omega\text{-cm}$ , and  $\mu_{300} = 2.9 \times 10^3 \text{ cm}^2 \text{ V}^{-1} \text{ sec}^{-1}$ .



Fig. III-2. Dependence of  $R_H T^{3/2}$  (left ordinate) and resistivity  $\rho$  (right ordinate) on reciprocal absolute temperature ( $1/T$ ) for a semi-insulating InP sample from an Fe-doped LEC boule.



the highest mobility so far reported for semi-insulating InP. The results of the measurements are shown in Fig. III-2, where  $R_H T^{3/2}$  and  $\rho$  are plotted on logarithmic scales vs reciprocal absolute temperature ( $1/T$ ). The activation energy obtained is 0.65 eV, in good agreement with published values of 0.66 eV (Ref. 5) and 0.68 eV (Ref. 6).

For samples from several recent Fe-doped boules,  $n$  at  $\sim 290$  K is plotted in Fig. III-3 as a function of the mole-fraction of Fe added to the growth charge. The number given beside each data point is the value of  $\rho$  at the same temperature in units of  $10^8 \Omega\text{-cm}$ . The curves shown in Fig. III-3 were calculated by assuming various values for the difference between  $N_D$ , the total donor concentration, and  $N_A$ , the concentration of acceptors other than Fe, and adopting  $1.6 \times 10^{-3}$  as the distribution coefficient for Fe in InP (Ref. 7) and 0.65 eV as the energy difference between the Fe level and the conduction-band edge. Comparison of the experimental points with these curves indicates that the values of  $(N_D - N_A)$  range from over  $5 \times 10^{15} \text{ cm}^{-3}$  to nearly  $4 \times 10^{16} \text{ cm}^{-3}$ . These values are surprisingly high in view of the fact that  $n_{300}$  in the most recent undoped LEC boules is less than  $5 \times 10^{15} \text{ cm}^{-3}$ . The additional donors might be due to small concentrations of contaminants in the Fe used for doping that have distribution coefficients much larger than that of Fe.

A number of p-type LEC boules with hole concentrations ( $p_{300}$ ) between about  $7 \times 10^{15}$  and  $8 \times 10^{18} \text{ cm}^{-3}$  have been obtained by loading elemental Zn or Cd into the BN crucible along with the polycrystalline charge, then proceeding with crystal growth in the usual manner. The hole mobilities ( $\mu = R_H/\rho$ ) at 77 and 300 K for samples from these Zn- and Cd-doped boules are plotted against  $p_{300}$  in Fig. III-4. Data are also shown for two samples with  $p_{300}$  of less than  $10^{16} \text{ cm}^{-3}$  from boules that were intentionally doped with Fe but also contained Zn due to

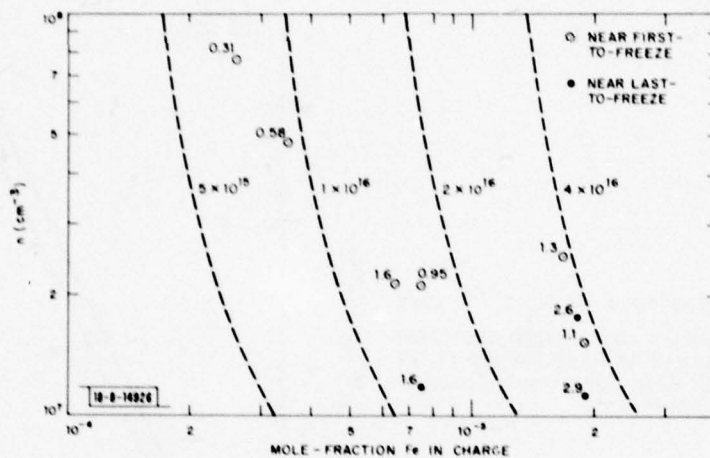


Fig. III-3. Electron concentration at 300 K ( $n_{300}$ ) for semi-insulating samples of InP as a function of mole-fraction of Fe added to LEC charge. Curves were calculated for indicated values of difference between total donor concentration and concentration of acceptors other than Fe.

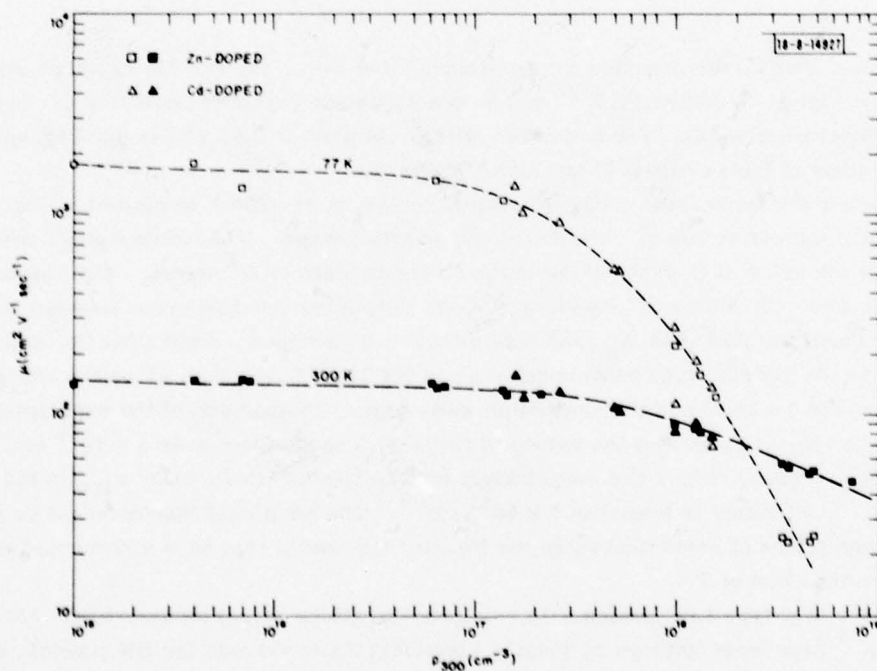


Fig. III-4. Hole mobilities ( $\mu$ ) at 77 and 300 K as a function of hole concentration at 300 K ( $p_{300}$ ) for p-type samples of InP from Zn- or Cd-doped LEC boules.

crucible contamination. The results in Fig. III-4 are in general agreement with earlier values.<sup>8,9</sup> The results for the lowest values of  $p_{300}$  indicate that the lattice mobilities for holes in InP at 77 and 300 K are at least 1800 and 150  $\text{cm}^2\text{V}^{-1}\text{sec}^{-1}$ , respectively. For hole concentrations exceeding about  $2 \times 10^{18} \text{ cm}^{-3}$ ,  $\mu_{77}$  is less than  $\mu_{300}$  because  $R_H$  is lower at 77 K than at 300 K, presumably due to impurity banding.

G.W. Iseler

#### B. LIQUIDUS DATA FOR LPE GROWTH OF $\text{Ga}_{0.47}\text{In}_{0.53}\text{As}$ ON InP SUBSTRATES

For optimum performance and reliability of optoelectronic devices fabricated from semiconductor heterostructures, the lattice constants of the epitaxial layers and the substrate forming these structures should be matched as closely as possible. The ternary alloy  $\text{Ga}_{0.47}\text{In}_{0.53}\text{As}$ , which has an energy gap of 0.75 eV (corresponding to a wavelength of 1.65  $\mu\text{m}$ ), has the same lattice constant as InP. Consequently, there is considerable interest in infrared devices utilizing lattice-matched heterostructures produced by using liquid-phase epitaxy (LPE) to grow  $\text{Ga}_{0.47}\text{In}_{0.53}\text{As}$  layers on InP substrates. Diode lasers,<sup>10-12</sup> photodiodes,<sup>13,14</sup> and photocathodes<sup>15</sup> have recently been fabricated from such heterostructures.

The LPE growth of  $\text{Ga}_{0.47}\text{In}_{0.53}\text{As}$  on (111)B-oriented InP substrates has been reported by several workers,<sup>10-12,16,17</sup> and growth on (100) substrates has also been achieved.<sup>12,18,19</sup> However, the data on the liquidus compositions and temperatures that result in deposition of lattice-matched layers are limited, and in some cases inconsistent. We have now determined liquidus data for growth on both substrate orientations over the temperature range between 540° and 720°C. For temperatures below about 690°C, these data confirm an earlier report<sup>19</sup> that different solution compositions are required for lattice-matched growth on the two orientations at the same temperature. By using accurate liquidus data, we are able to obtain high-quality layers as easily on (100) substrates as on (111)B substrates, although it has been reported previously that (100) growth is considerably more difficult.<sup>18</sup>

Liquidus-temperature ( $T_l$ ) determinations were made by the visual observation method.<sup>20</sup> For each measurement, a mixture of GaAs, InAs, and In with the desired composition was placed in the solution well of a horizontal graphite boat inside a transparent furnace. The mixture was heated until it became completely molten, cooled until spontaneous precipitation of  $\text{Ga}_x\text{In}_{1-x}\text{As}$  occurred, and then gradually reheated until the precipitates completely dissolved. The temperature at which the precipitates just disappeared was taken to be  $T_l$ .

To determine the alloy composition deposited from a given growth solution, LPE growth was carried out in a horizontal graphite slider boat by means of the supercooling technique.<sup>21</sup> A (111)B or (100) InP substrate was placed in the boat, the desired mixture of GaAs, InAs, and In was placed in the solution well, and the temperature was raised until the mixture became molten. The furnace was then cooled at a constant rate of 0.2°C/min. until the temperature reached about 6°C below  $T_l$ , the molten solution was placed in contact with the substrate, cooling was continued at the same rate until an epilayer about 5  $\mu\text{m}$  thick was formed, and the solution was pushed off the substrate. The lattice constant of the grown layer was measured with an x-ray diffractometer, using the diffraction lines of the substrate as an internal standard. We estimate that a lattice mismatch as small as 0.05 percent can be measured by this method. In some cases, the composition of the layer was measured by electron microprobe analysis. The epilayer lattice constant was found to increase by about 0.01 percent per micrometer in the



direction away from the substrate surface, but no composition variation could be detected with the microprobe even for layers more than 20  $\mu\text{m}$  thick. This result is consistent with the value of  $\pm 3$  percent usually adopted for the relative accuracy of microprobe analysis.

The experimental results for the LPE growth of  $\text{Ga}_x\text{In}_{1-x}\text{As}$  from Ga-In-As solutions are summarized in Table III-1, which lists the As and Ga concentrations in each growth solution, the value of  $T_f$ , the lattice mismatch between the grown layer and the substrate (defined as the lattice constant of the layer minus that of InP, divided by the lattice constant of InP), and the

TABLE III-1 EXPERIMENTAL DATA FOR LPE GROWTH OF $\text{Ga}_x\text{In}_{1-x}\text{As}$ ON InP					
Substrate Orientation	Composition of Liquid (a/o)		$T_f$ ( $^{\circ}\text{C}$ )	Lattice Mismatch* (percent)	Composition of Solid (x)
	As <sup>l</sup>	Ga <sup>l</sup>			
(111)B	2.49	2.34	577	0	0.470
	4.53	2.62	627	0	0.464
	8.75	3.00	691	0	—
	10.50	3.20	714	0	—
	2.07	1.31	544	+1.35	—
	2.62	2.62	579	-0.24	—
	4.63	2.82	631	-0.34	—
	7.40	3.00	676	-0.13	—
(100)	2.10	1.50	545	0	—
	2.80	1.70	572	0	0.486
	4.00	1.96	605	0	0.473
	5.70	2.42	640	0	—
	8.75	3.00	691	0	—
	10.50	3.20	714	0	—
	2.07	1.31	544	-1.47	—
	2.49	2.34	577	-2.68	—
	2.80	1.60	571	+0.14	—
	2.80	1.86	574	-0.24	—
	4.00	1.90	602	-0.09	—
	5.70	2.50	641	-0.08	0.494
	7.40	3.00	676	-0.34	—
* $100(a_{\text{GaInAs}} - a_{\text{InP}})/a_{\text{InP}}$					



layer composition if it was measured. Data for growth on (111)B and (100) substrates are grouped separately. The lattice mismatch is listed as zero for those cases in which it was too small to be measured. The layer composition was measured in four of these cases. To within the accuracy of the microprobe analysis, all the measured compositions agree with the value of  $x = 0.47$  previously reported<sup>10,16</sup> for the composition of  $\text{Ga}_x\text{In}_{1-x}\text{As}$  that is lattice-matched to InP.

For those growth solutions that yielded lattice-matched layers, the liquidus data are shown in Fig. III-5, where  $T_l$  (upper graph) and  $\text{Ga}^l$ , the concentration of Ga in the solution (lower graph), are plotted against  $\text{As}^l$ , the concentration of As in the solution. Figure III-5 also includes data previously reported by Nagai and Noguchi<sup>12</sup> and by Pearsall *et al.*,<sup>19</sup> which are in good agreement with the present results, and the data of Bachmann and Shay,<sup>14</sup> which are not.

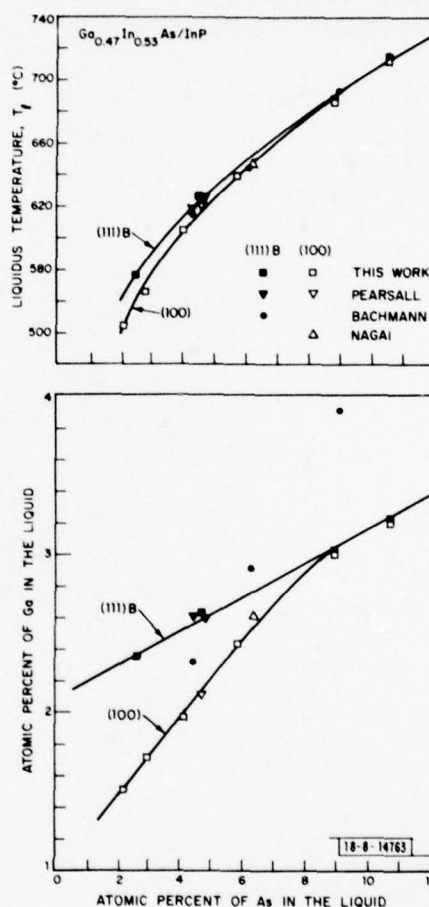


Fig. III-5. Liquidus temperature (upper graph) and Ga concentration in growth solution (lower graph) plotted against As concentration in growth solution for LEC growth of lattice-matched  $\text{Ga}_{0.47}\text{In}_{0.53}\text{As}$  epilayers on (111)B- and (100)-oriented substrates of InP.

The data in Fig. III-5 demonstrate a marked effect of substrate orientation on epilayer composition, which has been reported earlier for  $\text{Ga}_x\text{In}_{1-x}\text{As}$  (Ref. 19) and also for  $\text{Ga}_x\text{In}_{1-x}\text{As}_y\text{P}_{1-y}$  (Ref. 22). For both substrate orientations that we have investigated, lattice-matched growth has been obtained over a range of  $\text{As}^l$  values from about 2 to 11 a/o. In each case,  $\text{Ga}^l$  and  $T_l$  increase as  $\text{As}^l$  increases. For a given value of  $\text{As}^l$ , the values of  $\text{Ga}^l$  and  $T_l$  required for

lattice-matched growth at the highest temperatures are the same for both orientations. Below about 690°C, however, the required values of  $Ga^f$  and  $T_f$  are significantly higher for (111)B substrates than for (100) substrates, and the difference increases with decreasing temperature.

In experiments on the LPE growth of  $Ga_xIn_{1-x}P$  layers on GaAs substrates, it was observed that the lattice-matched composition was deposited from growth solutions covering a significant composition range.<sup>23</sup> The data of Table III-1 indicate that such preferential deposition of the lattice-matched composition ("lattice pulling") does not occur for the growth of  $Ga_xIn_{1-x}As$  layers on InP substrates, since even small changes in solution composition cause significant changes in epilayer composition. For example, for growth on (100) substrates from solutions with  $As^f = 2.80$  a/o, the lattice-matched composition was obtained for  $Ga^f = 1.70$  a/o, but a positive lattice mismatch was obtained for  $Ga^f = 1.60$  a/o and a negative mismatch for  $Ga^f = 1.86$  a/o. Our previous experiments on the growth of  $Ga_xIn_{1-x}As_yP_{1-y}$  layers on InP substrates also indicated the absence of lattice pulling.<sup>22</sup>

J. J. Hsieh

## REFERENCES

1. J. A. Rossi, J. J. Hsieh, and J. P. Donnelly, in Gallium Arsenide and Related Compounds (St. Louis) 1976, edited by L. F. Eastman, Conf. Ser. No. 33 B (The Institute of Physics, Bristol, 1977), p. 303  
DDC AD-A046991/6.
2. C. E. Hurwitz and J. J. Hsieh, Appl. Phys. Lett. **32**, 487 (1978).
3. J. B. Mullin, R. J. Heritage, C. H. Holiday, and B. W. Straughan, J. Cryst. Growth **3/4**, 284 (1968).
4. G. A. Antypas, in Gallium Arsenide and Related Compounds (St. Louis) 1976, edited by L. F. Eastman, Conf. Ser. No. 33 B (The Institute of Physics, Bristol, 1977), p. 55.
5. O. Mizuno and H. Watanabe, Electron. Lett. **11**, 118 (1975).
6. G. K. Ippolitova, E. M. Omelyanovskii, N. M. Pavlov, A. Y. Nashelskii, and S. U. Yakobsen, Sov. Phys. Semicond. **11**, 773 (1977).
7. R. N. Lee, M. K. Norr, R. L. Henry, and E. M. Swiggard, Mater. Res. Bull. **12**, 651 (1977).
8. M. Glicksman and K. Weiser, J. Phys. Chem. Solids **10**, 337 (1959).
9. K. J. Bachmann, E. Buehler, B. I. Miller, J. H. McFee, and F. A. Thiel, J. Cryst. Growth **39**, 137 (1977).
10. H. Nagai and Y. Noguchi, Appl. Phys. Lett. **29**, 740 (1976).
11. Solid State Research Report, Lincoln Laboratory, M.I.T. (1976:4), p. 41,  
DDC AD-A039175.
12. H. Nagai and Y. Noguchi, Appl. Phys. Lett. **32**, 234 (1978).
13. T. P. Pearsall and R. W. Hopson, Jr., J. Electron. Mater. **7**, 133 (1978).
14. K. T. Bachmann and J. L. Shay, Appl. Phys. Lett. **32**, 446 (1978).
15. J. S. Escher, P. E. Gregory, G. A. Antypas, R. Sankaran, and Y. M. Houng, J. Appl. Phys. **49**, 447 (1978).
16. R. Sankaran, R. L. Moon, and G. A. Antypas, J. Cryst. Growth **33**, 271 (1976).
17. T. P. Pearsall and R. W. Hopson, Jr., J. Appl. Phys. **48**, 4407 (1977).
18. S. B. Hyder, G. A. Antypas, J. S. Escher, and P. G. Gregory, Appl. Phys. Lett. **31**, 551 (1977).
19. T. P. Pearsall, R. Bisaro, R. Ansel, and P. Merenda, Appl. Phys. Lett. **32**, 497 (1978).
20. J. J. Hsieh, J. Electrochem. Soc. **121**, 99c (1974).
21. J. J. Hsieh, J. Cryst. Growth **27**, 49 (1974), DDC AD-A008298/2.
22. J. J. Hsieh, M. C. Finn, and J. A. Rossi, in Gallium Arsenide and Related Compounds (St. Louis) 1976, edited by L. F. Eastman, Conf. Ser. No. 33 B (The Institute of Physics, Bristol, 1977), p. 37,  
DDC AD-A046985/8.
23. G. B. Stringfellow, J. Appl. Phys. **43**, 3455 (1972).



## IV. MICROELECTRONICS

### A. MONOLITHIC SILICON BOLOMETERS

Broadband radiation detectors in the 1- to 30-cm<sup>-1</sup> band which will operate between 0.3 to 4.2 K are under development. For this purpose, a bolometer-type, silicon detector is being fabricated. The entire bolometer structure, illustrated in Figs. IV-1 and IV-2, is etched out of single-crystal, high-purity silicon wafers. The actual detector area, which is 5 mm × 5 mm × 10 μm thick, is suspended by four narrow silicon "spider" legs from a 150-μm-thick silicon frame. The spider legs are 3 mm long, and have a nominal 10-μm-thick × 50-μm-wide cross section. The resistance thermometer in the center is designed to have a uniform, 5-percent compensated net donor density of  $3.3 \times 10^{18} \text{ cm}^{-3}$  to a depth of 0.55 μm. This is accomplished by a series of five phosphorous implants, compensated by an additional series of five 5-percent compensating boron implants. The design goal is a device with a radiation noise equivalent power (NEP) of  $2 \times 10^{-15} \text{ W/Hz}^{1/2}$  at 1.5 K with a 1/30-sec time constant.

The silicon wafers used for this detector development are <100> float-zone silicon doped with phosphorus in the range 1000 to 200 ohm-cm. On each 150-μm-thick, 51-mm-diam wafer, four 15-mm-square bolometers are fabricated. To form 0.1-μm-deep ohmic contacts to the resistance thermometer, an initial arsenic implant of  $2 \times 10^{16} \text{ cm}^{-2}$  at 150 keV is implanted through a molybdenum/gold-on-SiO<sub>2</sub> mask. After an additional photolithography step, the compensating boron-implant series given in Table IV-1 is performed. The phosphorous-implant series given in Table IV-2 is performed next to achieve a net donor density in the  $3.5 \times 10^{18} \text{ cm}^{-3}$  range. All implants are then activated in the course of a passivation oxidation in steam at 900°C for 15 min. followed by a 15-min. anneal in N<sub>2</sub> also at 900°C.

At this point in the process, chrome-gold is deposited on both sides of the wafer, and the wafer is photolithographically processed and etched to form both the contacts to the As implants and the etch mask for the silicon thinning step. The resistors are then tested at 4.2 K, and normally exhibit a temperature variation approximated by

$$R(T) = R_0 \exp [T/T_0]^{-1/2}$$

where  $R_0$  and  $T_0$  are curve fitting parameters. Usable devices exhibit an  $R$  at 4.2 K of  $8 \times 10^4$  to  $4 \times 10^5$  ohms. Approximately 20 percent of all devices fabricated meet this criterion. The reasons for the low yield are currently under investigation. Two possible problems are ion implant nonuniformities, and incomplete activation of the entire series of implants at the activation temperature of 900°C.

Subsequent processing for the bolometers includes an isotropic silicon back etch of the active bolometer element to 5 to 10 μm, and a hydrazine anisotropic etch on the front side to form the spider support structure. The bolometer is completed by the evaporation of bismuth and SiO absorber layers on the back side of the active bolometer element (see Fig. IV-2).

PRECEDING PAGE BLANK



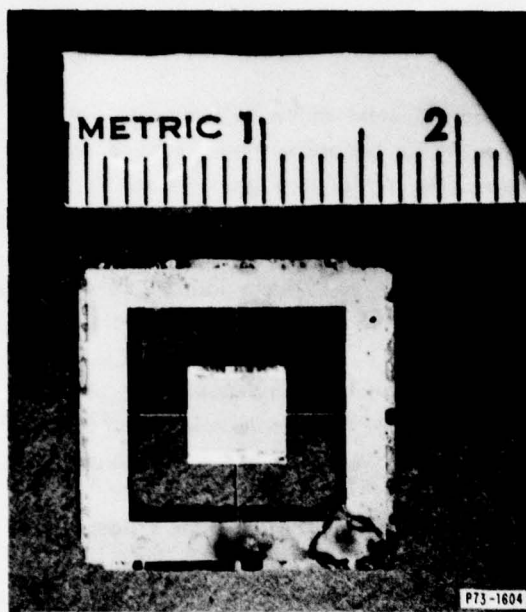


Fig. IV-1. Integrated silicon bolometer,  $15 \times 15$  mm. Outside frame is  $150 \mu\text{m}$  thick, while center resistance thermometer and "spider" legs are  $10 \mu\text{m}$  thick. Width of legs is  $50 \mu\text{m}$ . Bright bands at each of center section are gold contacts to resistance thermometer.

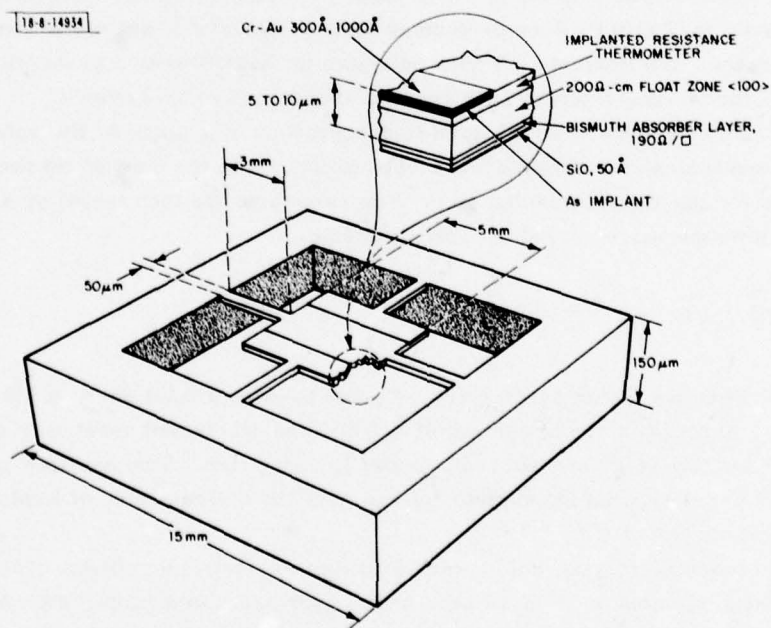


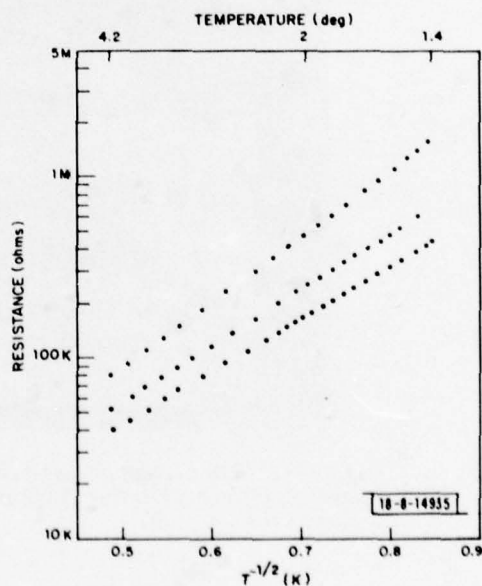
Fig. IV-2. Cross-sectional diagram of integrated silicon bolometer with detail of absorber and resistance thermometer.

TABLE IV-1 COMPENSATING BORON IMPLANT	
Boron Dose ( $\text{cm}^{-2}$ )	Ion Energy (keV)
$4.50 \times 10^{12}$	135
$2.74 \times 10^{12}$	80
$1.68 \times 10^{12}$	50
$1.06 \times 10^{12}$	33
$7.90 \times 10^{11}$	20

TABLE IV-2 PHOSPHOROUS-IMPLANT SERIES	
Phosphorous Dose ( $\text{cm}^{-2}$ )	Ion Energy (keV)
$8.75 \times 10^{13}$	400
$5.25 \times 10^{13}$	265
$3.32 \times 10^{13}$	160
$2.19 \times 10^{13}$	105
$1.40 \times 10^{13}$	65

The detectors that have been tested behave as expected from their resistance-vs-temperature curves and their geometry. Characteristics of some typical devices are given in Fig. IV-3. The time constants are independent of temperature from 4.2 to 1.5 K. The thermal conductivity vs temperature shows a  $T^3$  dependence and gives consistent values, both at high- and low-bias powers. The excess current noise ( $1/f$  noise) at optimum bias in the best detectors is less than the Johnson and phonon noise at frequencies greater than 5 Hz. These detectors have radiation NEPs in the range of a few times  $10^{-14} \text{ W/Hz}^{1/2}$  at 1.5 K with single time constants of a few milliseconds. With optimization of current fabrication techniques, including reduction of the

Fig. IV-3. Resistance dependence on temperature for three typical silicon integrated bolometers.  $T^{-1/2}$  exponential behavior is clearly demonstrated. Significant change in resistance in range below 4.2 K allows for very precise cosmic background radiation measurements.



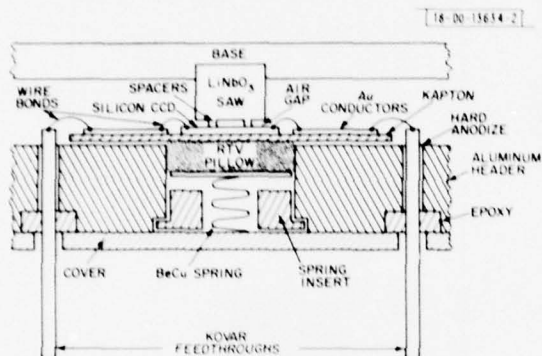


Fig. IV-4. Cross-sectional view of an assembled SAW/CCD buffer memory device. Header is attached to base with machine screws.

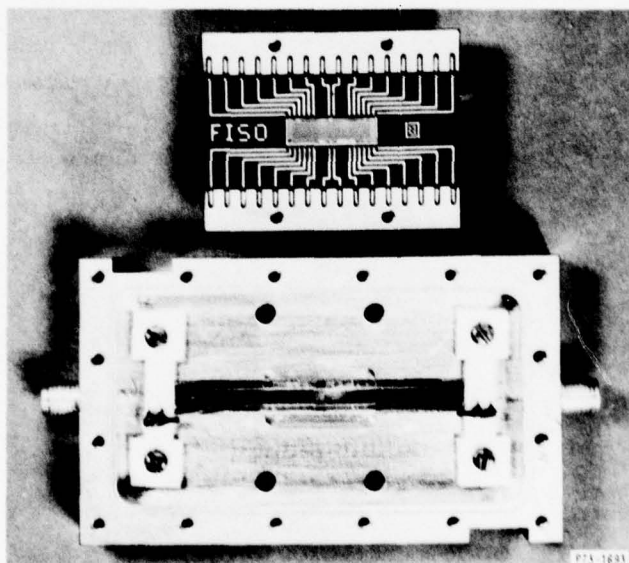


Fig. IV-5. Photograph of partially assembled SAW/CCD device including silicon CCD die, Kapton sheet, LiNbO<sub>3</sub> delay line, and metal parts.

detector thickness to  $5\text{ }\mu\text{m}$  and the spider leg cross section to  $25 \times 5\text{ }\mu\text{m}$ , the design goal radiation NEP of  $2 \times 10^{-15}\text{ W/Hz}^{1/2}$  at  $1.5\text{ K}$  with a  $1/30\text{-sec}$  time constant should be realized.

D. J. Silversmith	R. Weiss <sup>†</sup>
J. P. Donnelly	P. M. Downey <sup>†</sup>
R. W. Mountain	

#### B. CHARGE-COUPLED DEVICES: SAW/CCD BUFFER MEMORY

The first SAW/CCD buffer memory device<sup>4</sup> has been assembled, and evaluation of the completed unit is in progress. This report focuses on the details of the package design and assembly procedure.

The packaging of a SAW/CCD device is a challenging problem. Previous acoustoelectric devices such as the convolver or the memory correlator<sup>2,3</sup> do not require any connections to the front face of the silicon chip. However, in order for a CCD to operate, at least 12 connections must be made to the front surface. Furthermore, the metallization on a CCD is almost  $1\text{ }\mu\text{m}$  thick. If the gap between the propagating surface wave and the surface of the semiconductor is to have the required spacing of less than  $0.5\text{ }\mu\text{m}$ , then the lithium niobate ( $\text{LiNbO}_3$ ) SAW crystal must be made narrower than the silicon chip, in contrast to previous devices which utilized narrow silicon strips placed on top of a relatively wide SAW delay line. Care must also be taken that there is no metallization on the silicon in the region overlying the SAW crystal.

The scheme developed to solve these problems is based on the technique used for the convolver and for the memory correlator,<sup>2,3</sup> and is illustrated in Fig. IV-4. The assembly sequence is as follows. First the CCD die is epoxied to a gold pad on the Kapton sheet, and aluminum wires are ultrasonically bonded to pads on the CCD and to gold conductors on the Kapton. Then the Kapton is attached to the header, which has previously been fitted with gold-plated kovar leads.<sup>4</sup> Ultrasonically bonded aluminum wires are used to connect the conductors on the Kapton to the leads in the header. A photograph of a CCD silicon wafer, Kapton sheet, and header, assembled as described above, is shown in Fig. IV-5.

The  $\text{LiNbO}_3$  delay line has gap spacers and alignment marks that were ion-beam etched into the surface of the crystal. The crystal is mechanically ground into a dog-bone shape in order to leave room for the input transducer and a test transducer at the wide ends, while making the center section of the crystal (which will carry the surface wave over the silicon sampling fingers) narrow enough not to touch the thick metallization on the CCD portion of the chip. (If the SAW crystal were allowed to touch the CCD metallization, the gap would be determined by the metal rather than by the spacers on the SAW crystal.) The transducers are connected to the input matching inductors with ultrasonically bonded aluminum wires. Figure IV-5 shows a SAW crystal mounted on a base and ready to be mated with the silicon-Kapton header subassembly.

The silicon-header subassembly is placed in an assembly jig, and dust particles on the  $\text{LiNbO}_3$  crystal and silicon surface are completely removed by a variety of mechanical techniques (see Sec. V-B in this report). The  $\text{LiNbO}_3$  crystal is then accurately positioned over the silicon with the aid of alignment marks and pressed against the silicon. The package is filled with dry nitrogen and sealed.

---

<sup>†</sup> Department of Physics, M.I.T.



One device has been assembled as described, and the CCD and SAW devices have been separately evaluated. Final testing of the complete device awaits integration of the separate test setups.

D. L. Smythe    L. L. Grant  
R. W. Ralston    T. F. Clough

### C. CHARGE-COUPLED DEVICES: IMAGERS

The first hybrid arrays of  $100 \times 400$ -element CCD imaging devices have been fabricated for the GEODSS (Ground Electro-Optical Deep Space Surveillance) program. These arrays consist of two imaging chips mounted on a common substrate, and are to be used in the first tests of an optical moving target indicator (MTI) system for automatic satellite detection.

In previous reports,<sup>5</sup> a proposed hybrid array of  $100 \times 400$ -element CCD imagers was described consisting of 16 chips arranged in three columns. These chips must be precisely located on the substrate to the extent that the positional error of any chip is much less than the individual linear cell dimension of  $30 \mu\text{m}$ . By means of techniques previously described,<sup>5</sup> arrays of dummy chips have been assembled to within  $\pm 3\text{-}\mu\text{m}$  accuracy. Recent wafer runs of the CCD imagers have yielded chips of sufficient quality to begin assembling prototype arrays of two chips each. Photographs of the first such hybrid are shown in Figs. IV-6 and IV-7. In Fig. IV-6 the substrate with the two CCD chips is shown mounted in a 40-pin custom ceramic package. Outside dimensions of the package are  $6.1 \times 6.1 \text{ cm}$ . Details of the fabrication of the two-layer thin-film substrate carrying DC and clock lines are found in a previous report.<sup>6</sup> The three small chips to the right of each imager consist of the load resistor for the MOSFET

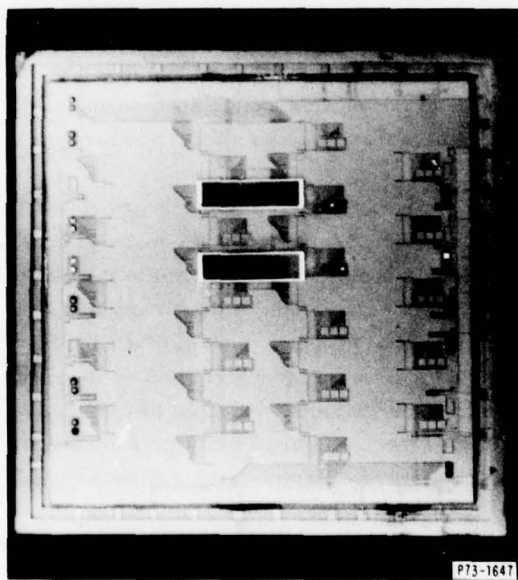


Fig. IV-6. Photograph of 2-chip CCD hybrid imaging array. Substrate is mounted in a 40-pin ceramic package and is designed to eventually accommodate 16 imaging chips.

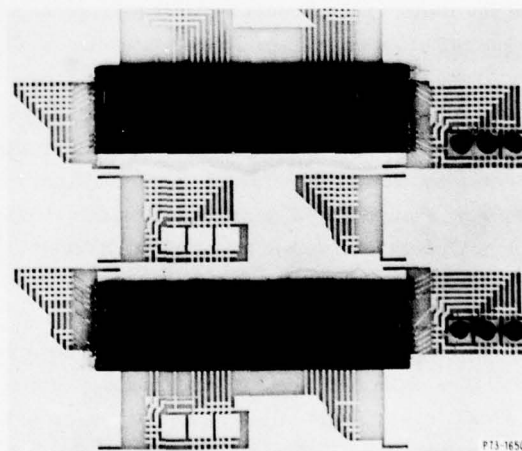


Fig. IV-7. Photograph of  $100 \times 400$ -element CCD chips of Fig. IV-6. These chips are positioned to an accuracy of  $4 \mu\text{m}$  with respect to each other. Clock and DC lines can be seen in two-level substrate. To right of each CCD is an emitter-follower circuit.

detector on the imager chip, and a bipolar transistor and load resistor in an emitter-follower configuration to drive the cable capacitance leading out of the Dewar in which the device will be mounted. Two of these arrays have been assembled; the placement accuracy of the chip pairs with respect to each other was within 4 and 10  $\mu\text{m}$ . The CCD chips are located slightly farther apart than the distance intended in the initial substrate design, the reason being that the separation between chips determines the memory size needed to store the video data from the first chip before comparison with the data from the second chip. The same  $100 \times 400$ -element devices are now being considered for use as the memory devices. Optimum use of this chip for data storage occurs when the imager chips are spaced such that the separation of corresponding cells on the two devices is an integral multiple of the Y-dimension length of the imaging area, or 0.120 in.

Measurements on recent devices had shown a marked improvement in transfer efficiency and output register dark current, while the imaging portion of the device still seemed to have dark currents in excess of  $100 \text{ nA/cm}^2$  (see p. 41 in Ref. 1). It has been discovered that the high dark currents are largely the result of a deep  $n^+$  diffusion kept on the back of the wafer throughout the process to provide gettering and inadvertently not removed at the end of the process. Electrons from this  $n^+$  layer can pass through the neutral p-type bulk of the device and be collected in the CCD channels at the top of the chip. This electron flow through the neutral bulk is governed by diffusion and can be calculated to be much less than  $1 \text{ nA/cm}^2$  of current. However, when the large-area imaging array gates pulse to their high state, they capacitively drive the p-substrate into temporary forward bias with respect to the  $n^+$  back-side skin. This causes a surge of electrons to flow into the p-bulk and enhances the net flow of electrons into the CCD wells. The effect could be eliminated by reverse-biasing the  $n^+$  layer with respect to the p-substrate, but the most convenient method for devices already packaged was to reduce the rising slew rate of the imaging array clocks to less than  $10 \text{ V}/\mu\text{sec}$ . Future devices, of course, will have the  $n^+$  skin removed before packaging. With the reduced rise-time clocks, devices previously found to have high dark currents have been measured to have dark currents as low as  $6 \text{ nA/cm}^2$  over the entire array with the exception of a few columns of dark current "spikes."

B. E. Burke	W. H. McGonagle
T. F. Clough	D. J. Silversmith
L. L. Grant	R. W. Mountain

#### D. CHARGE-COUPLED DEVICES: PROGRAMMABLE TRANSVERSAL FILTER

A prototype device consisting of two 1-bit, 32-tap CCD programmable transversal filter (PTF) sections which are capable of performing binary analog-sampled-data correlation has been tested. The device has performed matched filtering of a 31-bit, maximal (M) sequence<sup>7</sup> at a 10-MHz data rate.

A photomicrograph of the device is shown in Fig. IV-8. The chip size is  $0.106 \times 0.118$  in. This device has an on-chip serial-in/parallel-out, n-MOS static shift register for storage of a binary reference code. Multiplication of the analog input and binary reference is achieved using the logic states of the shift register to control the input-diode levels of the CCD. This input diode controls the signal-charge flow into the CCD channels.<sup>8</sup> If the shift register is at a logic-low state, signal charge can flow into the CCD channels, which corresponds to multiplying the analog signal by a "one." If the shift register is at a logic-high state, no charge can flow into the CCD channels, and multiplication by "zero" is performed. As can be seen in

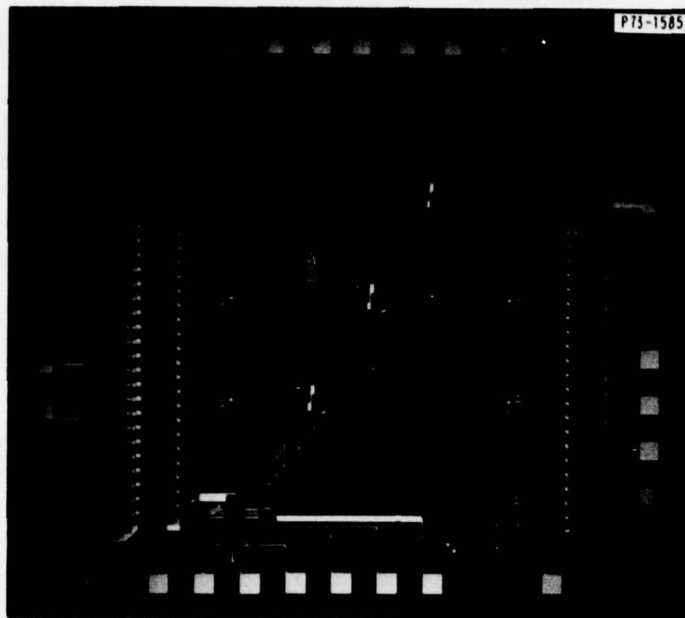
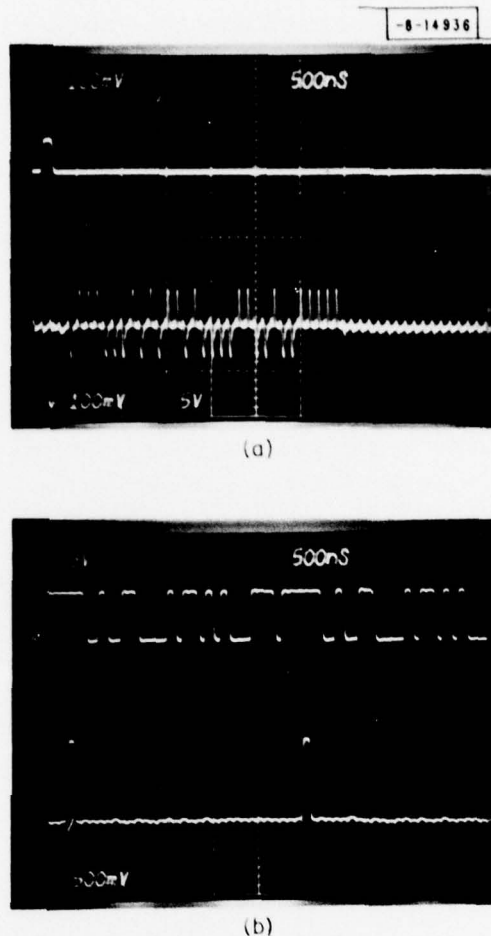


Fig. IV-8. Photograph of PTF chip containing two, 1-bit filter sections. Section on left incorporates shift register with static latch, while section on right uses output-enable switch to control input to CCD delay line.

Fig. IV-8, on the right-hand filter section an output-enable switch (see p. 56 in Ref. 3) is used as a buffer between the shift register and the CCD. On the left-hand section a latch circuit is included as a buffer store. Dynamic test results indicate that both versions of reference storage perform satisfactorily. However, for the right-hand filter the device is effectively not functional while a new reference code is being clocked into the shift register. When there is a reference latch, as in the left-hand filter, the device is capable of loading a new code while the correlation is being performed with a previously loaded code. Only 1  $\mu$ sec is required to parallel-transfer the reference from the shift register to the latch with an equivalent device "dead" time. The transfer time can be further reduced by reducing the depletion-layer capacitance of the CCD input diode. These results indicate that a CCD transversal filter with a shift register and latch store will be more practical for system applications where frequent reference code changes are required. Consequently, this version reference store is intended for use in the final 6-bit filters (see p. 56 in Ref. 3).

To demonstrate programmable matched filtering of a 31-bit, M-sequence, pseudonoise (PN) code, both filter sections were used. The 31-bit PN sequence was fed to one reference shift register, and its complement code to the other. These codes are serially loaded and permanently stored in the latch circuit of the left-hand filter and in the shift register of the right-hand filter. The outputs of the two sections are subtracted externally to establish the differential (+1, -1) weighting. The impulse response of the filter is shown in Fig. IV-9(a). The time-reversed sequence of the same code was then continuously fed to the CCD input-signal gates of both the left and right sections. The CCD devices are operated in such a way that a "zero" signal corresponds to a charge midway between the maximum charge,  $Q_{\max}$ , and the empty

Fig. IV-9. Example of programmable matched filtering using both sections of device in Fig. IV-8 at 10-MHz sampling rate; (a) shows impulse response of device. In (b), analog input to device corresponds to time-reversed reference code, which is equivalent to time-reversed impulse response, and resulting output gives autocorrelation for this code.



well. The analog signal charge in the  $k^{\text{th}}$  delay line,  $Q_{k,s}$ , can be either positive or negative and is given by

$$Q_{k,s} = Q_{k,t} - \frac{1}{2} Q_{\text{max}}$$

where  $Q_{k,t}$  is the total charge in the  $k^{\text{th}}$  delay line. The autocorrelation function of this M sequence is shown in Fig. IV-9(b). The peak-to-sidelobe ratio of this waveform is 31:1 as expected. The device has performed satisfactorily up to 10 MHz. Experiments are presently under way to test the device at an even higher data rate.

Some nonuniformity in the impulse response can be seen in Fig. IV-9(a). This "fixed pattern noise" has been observed in all the devices that have thus far been fabricated (see p. 56 in Ref. 3). A new fabrication run using epitaxial material is under way to determine if the threshold uniformity can be improved.

A. M. Chiang  
B. E. Burke  
D. L. Smythe



## E. CHARGE-COUPLED DEVICES: PROCESSING

Previous reports (Ref. 9; p. 47 in Ref. 6; and p. 46 in Ref. 1) have discussed methods and techniques for fabricating CCD devices. A series of developments in the GEODSS imager,<sup>10</sup> the PTF (see p. 47 in Ref. 6, p. 29 in Ref. 8, and p. 56 in Ref. 3), and the SAW/CCD buffer memory (see p. 37 in Ref. 1) programs make it timely to review our silicon-wafer-processing sequence. This sequence enables fabrication of buried-channel CCD devices with transfer efficiencies of 99.998 percent per stage, dark currents of less than  $6 \text{ nA/cm}^2$ , and generation lifetimes in excess of  $200 \mu\text{sec}$ . Furthermore, our processing allows us to integrate low-threshold voltage n-MOS FETs (n-channel metal-oxide-silicon field-effect transistors) required for peripheral circuitry such as shift registers and latches (see p. 43 in Ref. 1) on the CCD chips without any performance compromises.

The overall process resembles the LOCOS (local oxidation of silicon) procedure for MOS devices<sup>11-13</sup> in which the field oxide growth is prevented from forming in the active gate regions by a  $\text{Si}_3\text{N}_4$  oxidation mask. This same nitride layer can also serve as a diffusion mask for the formation of the channel stop in a self-aligned fashion. In our process, this nitride layer is also retained on the device to be used subsequently as the gate dielectric. The process is utilized currently for the PTF device, and will shortly be used in all CCD device programs. The simplest application of the procedure will be for the CCD/SAW buffer memory device. Slightly more complex processing is required for the PTF, as the peripheral circuitry requires shallow arsenic sources and drains for high-speed FETs and high reach-through voltage performance. The GEODSS imager, although requiring no arsenic implant, has three metallization levels (two polysilicon and one aluminum interconnect), a heavy channel-stop implantation, and an additional blooming-control implantation.

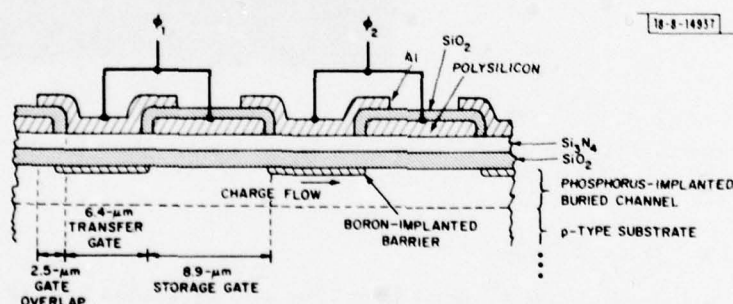


Fig. IV-10. Cross-sectional view showing two-phase CCD structure with  $10\text{-}\mu\text{m}$  polysilicon storage gates on first level, and  $6\text{-}\mu\text{m}$  aluminum transfer gates on second level.

The CCD topology for a buried-channel, two-phase structure is shown in cross section in Fig. IV-10. This configuration has four gates per CCD element – two storage gates on the first metal level and two transfer gates on the overlapping second level of metallization. In the direction of carrier motion (from left to right in Fig. IV-10), each transfer gate is connected to the subsequent storage gate. Within a CCD element, each transfer-gate/storage-gate pair is connected to the alternate driver clock phase. In order to assure unidirectional carrier motion, the channel potential of the transfer gate is higher than this same value for the storage gate. The channel voltage shift under the second-level transfer gate is accomplished by an ion

implantation (before deposition of the second-level metallization) using the first-level gates as an implant mask.

The important features of the CCD processing sequence can be illustrated by discussing the fabrication sequence for the PTF device. The starting material are Czochralski-grown, boron-doped  $\langle 100 \rangle$  Si wafers which are 51 mm diam by 380  $\mu\text{m}$  thick with a resistivity of 10 to 15 ohm-cm. The processing sequence begins with the "POGO" (pre-oxidation gettering of the other side) process (see p.46 in Ref. 1, and Refs. 14 and 15) which consists of a heavy phosphorous diffusion into the back side of the wafer [Fig. IV-11(a)]. As shown in Fig. IV-11(b), an overcoat of chemical-vapor-deposited  $\text{SiO}_2$  is applied which remains on the wafer throughout subsequent processing, serving to prevent outdiffusion of phosphorus and preventing impurity doping from the ambient. This oxide layer, along with the  $\text{n}^+$  POGO layer, can be removed after the device processing is finished.

Front-side processing commences with a thorough scrubbing and a cleaning step. A thin  $\text{SiO}_2$  film is grown in a dry  $\text{O}_2/\text{HCl}$  ambient at 1000°C, followed by the CVD deposition of  $\text{Si}_3\text{N}_4$ , forming a double-level gate dielectric layer. Photoresist is spun on [Fig. IV-11(c)] and the active channel region is defined. The nitride and thermal oxide layers are removed outside the channel region by means of plasma etching and aqueous etching in buffered HF. The boron channel-stop implantation is now performed utilizing the retained photoresist as a self-aligned implant mask, and will result in 24-V field threshold and breakdown voltages (see p.47 in Ref. 6). After the implantation, the photoresist is stripped in an  $\text{O}_2$  plasma. The field oxide is grown using a burnt hydrogen furnace at 1000°C, during which time the implant is activated [Fig. IV-11(d)]. The  $\text{Si}_3\text{N}_4$  layer serves as an effective oxidation mask in conformity with LOCOS processing.<sup>11,12</sup> In our variation of this processing sequence, however, the initial thin thermal oxide and CVD  $\text{Si}_3\text{N}_4$  films are retained to serve as the gate dielectric.

In order to improve performance above 1 MHz and to minimize transfer inefficiency due to surface states, the CCD devices are designed to operate in the buried-channel mode. This buried channel is fabricated by ion implantation of phosphorus right through the gate dielectric utilizing negative photoresist as an implant mask [Fig. IV-11(e)].

The need for compatible, compact n-MOS logic on the CCD device places stringent requirements on the nature of the source and drain doping. Using photolithographic and plasma-etch methods, the diode window is etched through the  $\text{Si}_3\text{N}_4$ , and arsenic is implanted through the gate oxide, as shown in Fig. IV-11(f). To heal any possible pinholes at this stage in the process, a steam oxidation at 900°C is performed.

Using an RF-heated cold-wall system, a film of silicon is now deposited on the wafer and will eventually form the first-level, storage-gate metallization. This film is doped with phosphorus to a sheet resistance of 50  $\Omega/\square$  measured after device completion [Fig. IV-11(g)]. Typically, photolithographic formation of the silicon gates takes place after doping of the polycrystalline silicon film.

The source and drain contacts are opened next as a matter of convenience, and the potential barrier which is to be under the second-level aluminum transfer gate is implanted. This barrier is implanted through the  $\text{SiO}_2/\text{Si}_3\text{N}_4$  [Fig. IV-11(h)]. The implant is designed to provide a channel potential shift of 2.3 V. To form a dielectric on top of the first metallization level, the polysilicon is oxidized and subsequently annealed. After this step, all contact windows are opened using a double-masking procedure to minimize pinhole problems.

Aluminum is deposited using an RF induction heated BN crucible which results in alkali-free films with no radiation damage<sup>16</sup> to the gate oxide. The aluminum is etched photolithographically

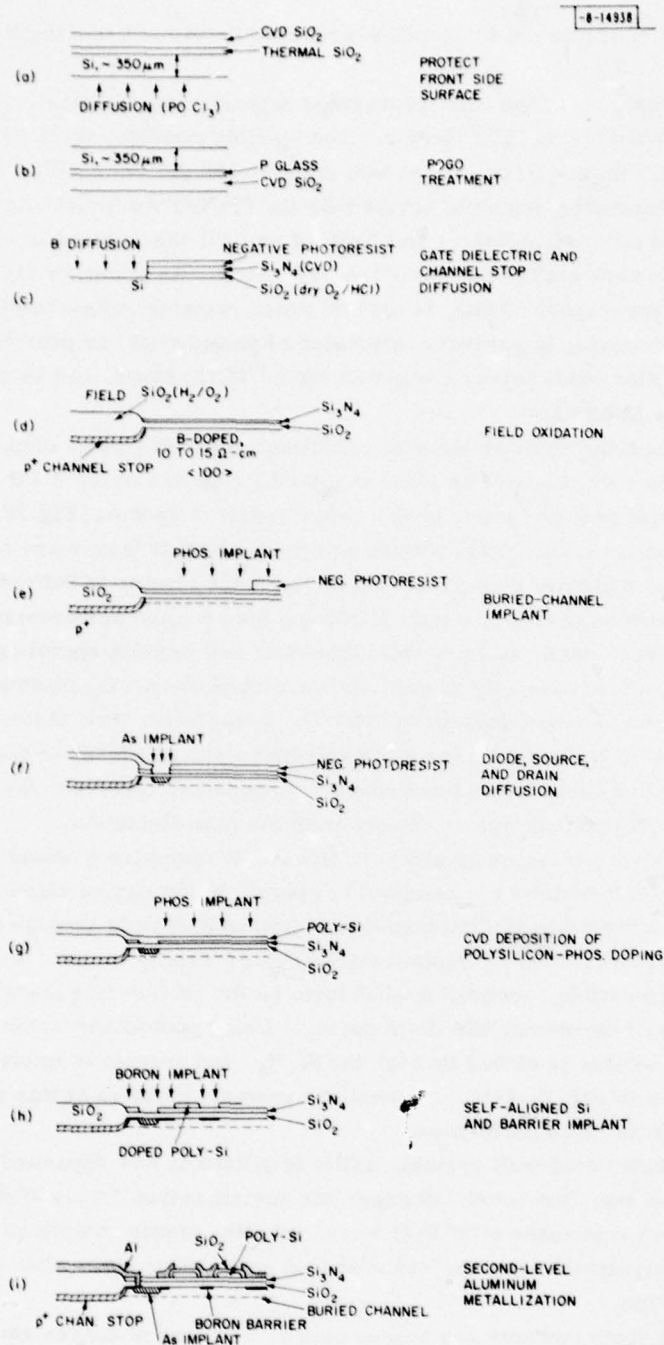


Fig. IV-11(a-i). Pictorial description of PTF processing sequence.



using a  $\text{H}_3\text{PO}_4\text{-HNO}_3$  mixture, and is sintered in  $\text{N}_2$  [Fig. IV-11(i)]. A CVD  $\text{SiO}_2$  layer is deposited as a passivation layer, and the bonding pads are opened by a final photolithographic step.

In summary, a nine-mask-step, two-phase, buried-channel CCD process has been developed using a variation of the LOCOS procedure. In this process, the composite gate dielectric of thin thermal  $\text{SiO}_2$  and CVD  $\text{Si}_3\text{N}_4$  is fabricated as a first step, with the field oxide grown subsequently. POGO gettering prepares the initial wafers before front-side processing, and this back-side gettering layer is retained until process completion. Ion implantation is utilized extensively, with two implants passing through the active gate dielectric without deleterious effects. The process is n-MOS compatible giving high punch-through and low back-gate-bias voltages. Shallow arsenic implants are used for source and drain diffusions. Aluminum deposited from an induction heated source serves as a second metallization.

D. J. Silversmith    B. E. Burke  
R. W. Mountain    A. M. Chiang

#### F. ALIGNMENT OF LIQUID CRYSTALS USING SUBMICROMETER PERIODICITY GRATINGS

Several researchers have demonstrated that surfaces which have been made anisotropic by rubbing with abrasives,<sup>17</sup> by directed oblique evaporation of silicon monoxide,<sup>18</sup> or by dipping in surfactants<sup>19</sup> will align nematic liquid crystals. We believe that such alignment minimizes the free energy associated with elastic deformation of the liquid crystal. In particular, if the long axes of the liquid crystal molecules are constrained to lie in, or at a small tilt angle to, the plane of a smooth surface, then one expects a grating structure on that same surface to induce alignment of the nematic director along the groove direction. Berreman<sup>20,21</sup> had earlier proposed a detailed model which lends support to this idea.

Oblique evaporation and rubbing techniques produce surfaces with a topography that is largely uncontrolled and, thus, is difficult to reproduce or quantify exactly. We demonstrate here that liquid crystals can be aligned on gratings whose topography is directly controlled. It is significant that the spatial period of the gratings used was 320 nm, which is much larger than the size of the molecules ( $\approx 2$  nm) being aligned. We expect the forces which favor alignment to increase with gratings of higher spatial frequency.

The gratings for the following experiments were fabricated in  $\text{SiO}_2$  by reactive ion etching in  $\text{CHF}_3$  gas using a mask of 100-Å-thick chromium. The chromium grating was produced by a liftoff process from a grating pattern exposed in PMMA using  $\text{Cu}_L$  soft x-ray lithography.<sup>22</sup> Holographic lithography was used as the pattern-generation step in producing the x-ray mask. The etch depth of our  $\text{SiO}_2$  gratings was about 25 nm. Recent measurements in a transmission electron microscope on gratings fabricated by this process indicate that the sidewalls are within  $6^\circ$  of the vertical, and that the radius of curvature at the top and bottom corners of the sidewalls is less than 5 nm. Gratings were fabricated over a  $1.25 \times 1.25$ -cm area on two highly polished fused quartz substrates.<sup>†</sup> The two substrates were assembled into a sandwich with 50- $\mu\text{m}$ -thick Teflon spacers holding them apart, as shown in Fig. IV-12. The gratings were on the inside of the sandwich and faced each other with their groove directions parallel. A high degree of parallelism is easily obtained by first roughly aligning the gratings so that a beam of light incident on them is simultaneously diffracted from both gratings toward an observer; then, fine adjustments in the alignment can be made while observing moiré interference fringe patterns in the overlapping diffracted beams.

<sup>†</sup>Optosil 2, Amersil Inc.



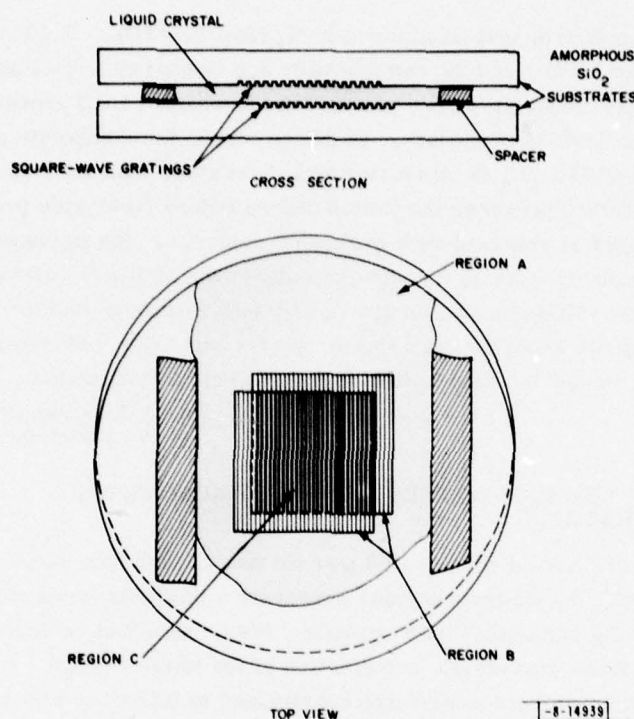


Fig. IV-12. A schematic cross section and top view are shown of the "sandwich" assembly used to investigate surface-relief structure orientation effects in nematic and smectic A liquid crystals.

After alignment of the gratings, the sandwich was heated above the nematic-isotropic transition temperature of MBBA [N-(p-methoxybenzilidene)-p-butylaniline] and the liquid crystal was introduced into the sandwich by capillary action. The sandwich was allowed to cool to room temperature where MBBA is nematic, and was observed in transmission in a microscope between crossed polarizers. The incident polarized light was normal to the thin liquid-crystal layer, and the entire sandwich could be rotated in the plane of the layer.

An aligned liquid crystal behaves as an optically uniaxial medium with its optic axis in the direction of the nematic director. When a linearly polarized beam of light is normally incident on a uniaxial slab of arbitrary thickness, it will remain linearly polarized after passing through the medium only if the polarization is perpendicular to the optic axis or parallel to the projection of the optic axis on the slab. In the area between the two gratings, distinct peaks and nulls in the light transmission were observed as the sandwich was rotated, the nulls occurring every 90°. Furthermore, the entire liquid-crystal layer in the grating area had a uniform brightness, with nulls in the light transmission occurring simultaneously across the entire field of view. Our interpretation is that the nematic director is not perpendicular to the substrates and that it is uniformly oriented in the grating area. The liquid-crystal layer had a distinctly different appearance in the region outside the grating area where it was confined between two smooth surfaces. It did not appear uniform, and many small domains were visible, indicating that the direction of the nematic director varies randomly in this region. The light transmission in the grating area went through a null when the incident polarization was along the groove direction, to within the experimental error of our apparatus (0.5°). This indicates that the projection of

the nematic director was aligned along the groove direction or perpendicular to it. In order to distinguish these two possibilities, we doped the MBBA with the dye DODCI (3, 3' diethyloxadicarbocyanine iodide) which aligns with the nematic director and absorbs most strongly light that is polarized in the direction of alignment. In this way, we established that the nematic-director projection was along the groove direction.

The angle between the nematic director and the plane of the substrate was estimated by measuring the difference between the refractive index for the ordinary wave and the extraordinary wave with light normally incident on the substrate. The extraordinary index varies with the angle between the incident ray and the optic axis. To make the measurement, one of the Teflon spacers was removed, thereby introducing a known tilt between the two quartz substrates. When viewed at normal incidence in monochromatic light (589 nm) between crossed polarizers, distinct dark and light bands were visible due to the linear variation in thickness of the birefringent medium. The dark bands occur when the relative phase shift between ordinary and extraordinary waves is an integral number of cycles. Knowing the tilt between the two substrates, the difference in index of refraction can be calculated from the spacing of the bands.<sup>23</sup> We measured an index difference of  $0.18 \pm 10$  percent. This corresponds to a nominal tilt of  $23^\circ$  between the nematic director and the substrate plane; this was the same inside and outside the grating area. For the tilt calculation, we used the value of  $0.225 (\pm 0.006)$  for the birefringence of MBBA at  $25^\circ\text{C}$ , which is correct if the nematic-isotropic transition temperature is in the range of  $41^\circ$  to  $45^\circ\text{C}$  (see Ref. 23). The transition temperature is sensitive to the purity of the liquid crystal and typically drops slowly when MBBA is first exposed to air, with a corresponding decrease in the birefringence. Though we did not measure it, the transition temperature is usually in the range of  $41^\circ$  to  $45^\circ\text{C}$ . Furthermore, conoscopic examination of our sample confirmed that the nematic director was tilted at least  $20^\circ$  from the substrate plane.

Surface contamination can make the nematic director approach the substrate normal, and thus degrade the orienting influence of the grating. Freshly made substrates and those cleaned in UV-generated ozone<sup>24</sup> or concentrated  $\text{H}_2\text{SO}_4$  exhibited good alignment, low tilt angle, and consistent results. Both highly polished fused quartz and  $\text{SiO}_2$  prepared by thermal oxidation of silicon wafers showed similar results.

We also aligned the liquid crystal M24 (BDH Chemicals Ltd., 4-cyano-4'-octoxybiphenyl), which has a smectic A as well as a nematic phase. We found that M24 in the nematic phase aligned uniformly along the groove direction in the grating area, but it exhibited a slowly varying nematic director outside the grating area where it was not constrained. The effect of the grating was striking when the liquid crystal was cooled to the smectic phase. The liquid crystal in the grating area appeared as a uniform uniaxial slab with the projection of its optic axis parallel to the groove direction; outside the grating area, a multitude of striations and fan-shaped defects appeared. No striations were visible in the area confined between two gratings.

Based on the above results, we have constructed a novel type of twisted nematic display using grating technology. Gratings of 100-nm-thick gold lines and 320-nm period were fabricated on a 225- $\mu\text{m}$ -thick Corning 0211 glass substrate using holographic lithography and ion-beam etching. The gold grating lines were interconnected by a continuous gold film which surrounded the grating area. Two of these 0211 glass pieces were assembled into a sandwich using Teflon spacers to maintain a gap between them. The gratings, which were inside the sandwich, were oriented with their groove directions perpendicular to each other. Electrical

contact was made to each gold surface. All the elements of a twisted nematic display are present in this structure: (1) the gratings provide two liquid-crystal-aligning surfaces at right angles to one another, (2) the gratings polarize light and act as crossed polarizers, and (3) the gratings are highly conductive at DC and form effective conducting parallel plates to align the liquid crystals by means of an electric field. The contrast ratio of the polarizer limits the performance of the display. Contrast ratios of 10:1 have been obtained using He-Ne laser light (632.0 nm). Improvements should be obtained with gratings of finer spatial period.

In conclusion, we have demonstrated that square-wave-grating surface-relief structures can be used to align nematic and smectic liquid crystals. Since these structures are well controlled and characterized, they permit quantitative models for alignment of liquid crystals by surfaces to be tested. Finally, surface structures may find wide application in other systems where anisotropic surface interactions are present.

D. C. Flanders  
D. C. Shaver  
H. I. Smith



## REFERENCES

1. Solid State Research Report, Lincoln Laboratory, M.I.T. (1977:4), pp. 37-39, DDC AD-A052463.
2. S. A. Reible, J. H. Cafarella, R. W. Ralston, and E. Stern, "Convolver for DPSK Demodulation of Spread Spectrum Signals," in 1976 Ultrasonics Symposium Proceedings (IEEE, New York, 1976), pp. 451-455, DDC AD-A040519/1.
3. Solid State Research Report, Lincoln Laboratory, M.I.T. (1976:4), pp. 73-74, DDC AD-A039175.
4. Ibid. (1975:2), p. 50, DDC AD-A013103/7.
5. Ibid. (1975:4), pp. 46-48, DDC AD-A025489/6; and (1976:2), pp. 47-48, DDC AD-A030861/9.
6. Ibid. (1977:2), pp. 50-53, DDC AD-A044795.
7. C. E. Cook and M. Bernfeld, Radar Signals (Academic Press, New York and London, 1967).
8. Solid State Research Report, Lincoln Laboratory, M.I.T. (1977:1), p. 29, DDC AD-A041226/2.
9. Ibid. (1976:1), p. 59, DDC AD-A027261/7.
10. Ibid. (1977:4), p. 39; (1977:2), p. 49; (1977:1), p. 31; and (1976:4), p. 53.
11. E. Kooi, J. van Lierop, W. Verkuijlen, and R. de Werd, Philips Res. Rep. 26, 166 (1971).
12. E. Kooi and J. Appels in Semiconductor Silicon 1973, H. Huff and R. Burgess, Eds. (The Electrochemical Society, Princeton, New Jersey, 1973), p. 860.
13. R. A. Cohen and R. W. Mountain, IEEE Trans. Electron Devices ED-18, 54 (1971), DDC AD-723787.
14. G. A. Rozgonyi, P. M. Petroff, and M. H. Read, J. Electrochem. Soc. 122, 1725 (1975).
15. G. A. Rozgonyi and R. A. Kushner, J. Electrochem. Soc. 123, 570 (1976).
16. G. F. Derbenwick, J. Appl. Phys. 48, 1127 (1977).
17. L. T. Creagh and A. R. Kmetz, Mol. Cryst. Liquid Cryst. 24, 59 (1973).
18. J. L. Janning, Appl. Phys. Lett. 21, 173 (1972).
19. J. E. Proust, L. Ter-Minassian-Saraga, and E. Guyon, Solid State Commun. 11, 1227 (1972).
20. D. W. Berreman, Phys. Rev. Lett. 28, 1683 (1972).
21. ———, Mol. Cryst. Liquid Cryst. 23, 215 (1974).
22. D. C. Flanders, H. I. Smith, H. W. Lehmann, R. Widmer, and D. C. Shaver, Appl. Phys. Lett. 32, 112 (1978).
23. I. Haller, H. A. Huggins, and M. J. Freiser, Mol. Cryst. Liquid Cryst. 16, 53 (1972).
24. J. R. Vig, IEEE Trans. Parts, Hybrids, and Packaging PHP-12, 365 (1976).



## V. SURFACE-WAVE TECHNOLOGY

### A. FILTER WITH BANDWIDTH CONTINUOUSLY VARIABLE FROM 3 TO 100 MHz

The variable-bandwidth filter<sup>1,2</sup> is being developed for use with a digital signal processor. The function of the filter is to prevent aliasing, i.e., to appropriately limit the bandwidth of an analog signal before it is sampled at the input of a digital system which has a variable sampling rate. The filtering is to be done around a center frequency of 600 MHz, with the bandwidth variable from 3 to 100 MHz.

The principle of operation of the filter is shown in Fig. V-1. The filter consists of two similar stages, each with a RAC (reflective-array-compressor) device between two mixers. By varying the two LOs, the overlap of the two RAC passbands effectively seen by the input can be varied.

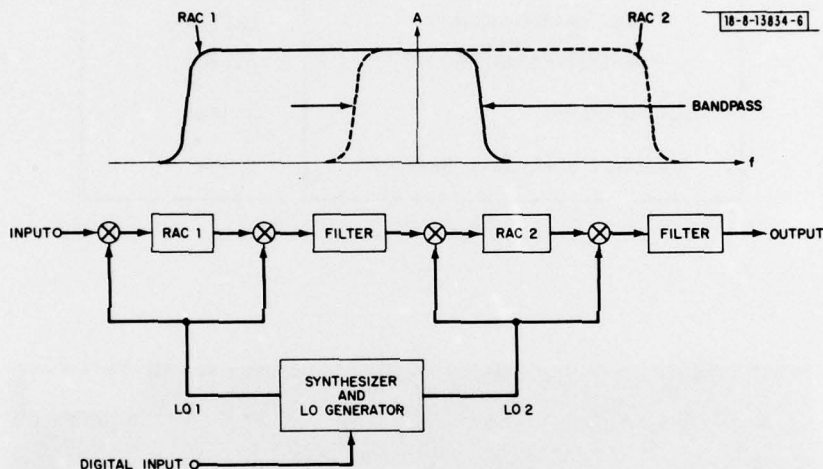


Fig. V-1. Schematic of variable-bandwidth-filter circuit. When two LO frequencies are equal, full 100-MHz bandwidth is transmitted from input to output. If one LO is shifted upward and one downward, RAC passbands are offset with respect to each other and passband is reduced as shown by curves at top.

For a variable-bandwidth filter to be useful, the filter bandwidth must vary over a wide range or, equivalently, the ratio of maximum to minimum bandwidth must be large. Because the minimum bandwidth in the filter circuit shown in Fig. V-1 is predominately determined by the steepness of skirts of the individual filters, the performance of the system is directly determined by the squareness or shape factor of the filters. Calculations, as well as past experience,<sup>3</sup> indicate that the RAC devices have the required shape factor and are of reasonable size. In addition, RAC devices can be trimmed for precise phase response.

The RAC center frequency and the two LO frequencies were chosen to minimize spurious signals. The best choice was  $f_0 = 420$  MHz, and the ranges of frequency variation of the two LOs were 1020 to 970 and 1020 to 1070 MHz. In this scheme, one RAC must be an up-chirp and one a down-chirp so that the overall filter can be nondispersive. The filter could also be

TABLE V-1 VARIABLE-BANDWIDTH-FILTER SUBSYSTEM	
Bandwidth Range	3 to 100 MHz
Passband Flatness	$\pm 1.5$ dB
Band-Edge Falloff -3 to -40 dB	3.5 MHz
Out-of-Band Rejection	63 dB
Dynamic Range	56 dB
Two-Tone Intermodulation Level	-40 dB
Delay	
Maximum Bandwidth	23.5 $\mu$ sec
Minimum Bandwidth	7.5 $\mu$ sec
Switching Time	35 $\mu$ sec
Phase Error at Maximum Bandwidth	5° rms

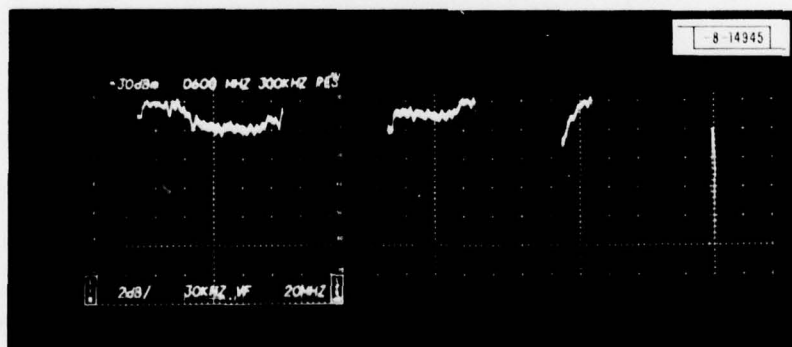


Fig. V-2. Passband of variable-bandwidth filter at bandwidths of 100, 60, 20, and 3 MHz. For all bandwidths, insertion loss is constant to within  $\pm 1.5$  dB. Vertical scale for all traces is same, 2 dB/div. Horizontal scale is 20 MHz/div.

operated with two down-chirp RACs, but then one of the LOs would have to be below 600 MHz, e.g., variable from 130 to 180 MHz. This leads to unacceptably high spurious levels because low-order harmonics of the LO produce strong unwanted in-band signals in the mixers.

The RACs for the circuit (Fig. V-1) were built with minimum insertion loss (approximately 30 dB), and the dynamic range of the circuit was optimized using off-the-shelf components. The individual RAC devices were phase-compensated to minimize deviations from the desired quadratic phase response.

The performance of the variable-bandwidth filter is summarized in Table V-1. The pass-band for several bandwidths is shown in Fig. V-2, while the phase response is shown in Fig. V-3 for three bandwidths.

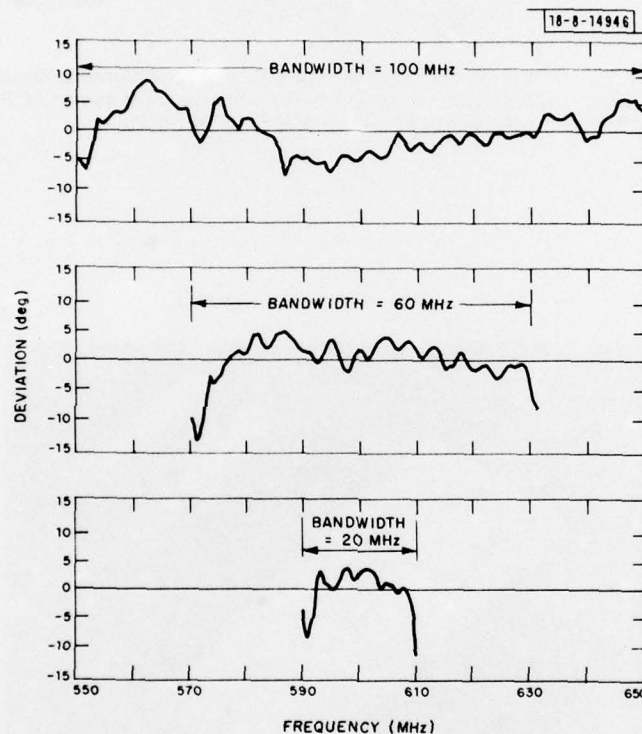


Fig. V-3. Phase deviation from linear of variable-bandwidth filter as a function of frequency. Both RACs were phase-compensated.

The delay through the variable-bandwidth filter is a function of the bandwidth selected, but at each bandwidth the delay is independent of frequency, except for the small residual variation shown by the phase measurements (Fig. V-3). With improved RAC devices currently being built, it appears likely that the passband ripple can be reduced to  $\pm 1$  dB and the phase deviation from ideal held to less than  $2^\circ$  rms. The other characteristics (Table V-1) meet or exceed the desired specifications.

J. Melngailis

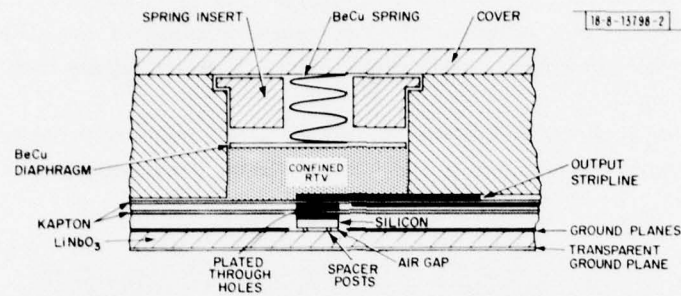


Fig. V-4. Cross-sectional view of gap-coupled acoustoelectric structure. Beryllium-copper springs act against layer of RTV to apply uniform pressure to back side of silicon.

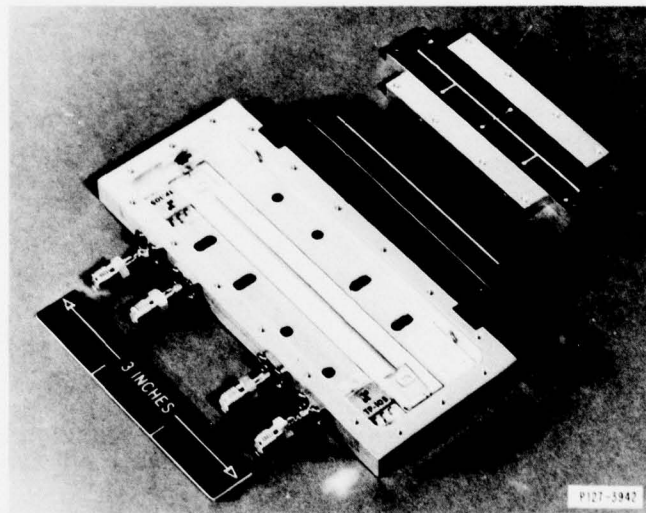


Fig. V-5. Three principal acoustoelectric device subassemblies - LiNbO<sub>3</sub> delay line in base, silicon-Kapton sheet, and connector plate.



## B. ASSEMBLY OF GAP-COUPLED ACOUSTOELECTRIC DEVICES

The gap-coupled acoustoelectric devices being developed at Lincoln Laboratory<sup>4-7</sup> consist of a lithium niobate ( $\text{LiNbO}_3$ ) delay line and a silicon strip separated by an intervening air gap. These devices require air-gap heights of 0.2 to 0.6  $\mu\text{m}$ , which must be uniform to  $\pm 0.01 \mu\text{m}$  over lengths up to 7 cm. The silicon is supported by an array of long narrow rails<sup>8,9</sup> (or a pseudo-random pattern of posts) which are fabricated by ion-beam etching the surface of the  $\text{LiNbO}_3$  delay line. The silicon is held against the rail supports by an RTV pillow and a series of springs,<sup>10</sup> as shown in Fig. V-4. This configuration maintains a stable air gap over a wide temperature range ( $-25^\circ$  to  $+75^\circ\text{C}$ ).

A specialized gap-assembly procedure was developed for the gap-coupled acoustoelectric devices. The four major requirements on the gap-assembly procedure are: (1) all particulate contamination having diameters greater than several tenths of a micrometer must be removed from the silicon and acoustic delay line; (2) the narrow (0.7- to 1.7-mm-wide) silicon strips have to be mounted to facilitate handling and electrical connection, without sacrificing mechanical flexibility; (3) the silicon must be aligned to tolerances of  $\pm 25 \mu\text{m}$  over an acoustic beam path having widths of 0.7 to 1.7 mm; and (4) it must be possible to test the major subassemblies before final gap assembly. In addition, one device<sup>10</sup> required the placement and precise alignment of two 3.5-cm silicon strips end-to-end.

The first step of the assembly procedure is a thorough cleaning of the  $\text{LiNbO}_3$  delay line to remove all particles which might otherwise interfere with obtaining an accurate and uniform gap. Further assembly is performed under clean conditions in order to avoid further particulate contamination. After cleaning, the delay line is mounted in its base (Fig. V-5) where electrical connections are made to the input matching circuitry. The delay line is then electrically tested prior to final gap assembly.

The silicon strip for an acoustoelectric device is prepared by metallizing the back of a silicon wafer and then saw cutting the wafer into strips of the desired size. Indium is evaporated onto the back side of the strips in preparation for indium bonding to a flexible Kapton<sup>†</sup> sheet which contains the required patterns for connecting the silicon strip to external circuitry. Indium is electroplated onto a metallized area of the Kapton sheet in preparation for bonding the silicon strip to this area. When the silicon strip is properly aligned over this area, pressure is applied in the presence of HCl flux and a cold weld is formed.

After the silicon strip is bonded to the Kapton, it is accurately aligned with and fastened to a connector plate which contains the output circuitry. The silicon surface is then carefully cleaned, and the connector plate (see Fig. V-5) is mounted in the assembly jig (Fig. V-6). Next, the delay-line subassembly is inverted and mounted on the assembly jig over the connector plate which holds the silicon-Kapton sheet. A slot in the back side of the delay-line package allows the silicon strip to be viewed as it is maneuvered into precise alignment over the acoustic beam path. After alignment, the connector plate is fastened to the delay-line base.

The final assembly step is the insertion of the RTV pillow, spring holder, and small springs into the back side of the connector plate (see Fig. V-7). A spring-pressure plate is then fastened to the connector plate to provide the proper spring compression. The device is finally sealed with two cover plates using indium-wire gaskets.

<sup>†</sup> Registered trademark: E. I. duPont Company.

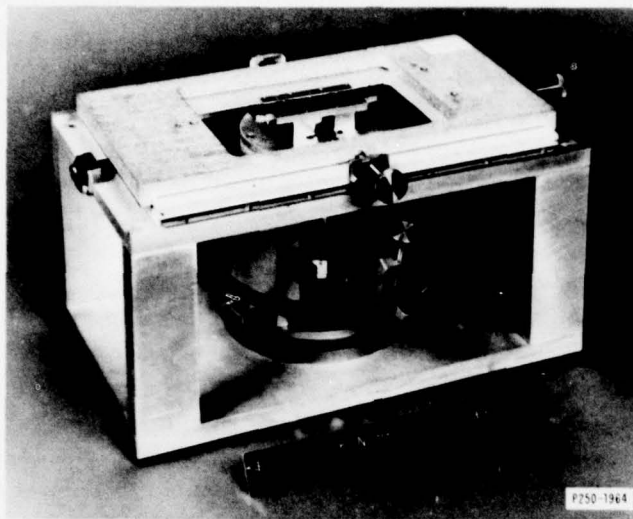


Fig. V-6. Assembly jig with connector plate.

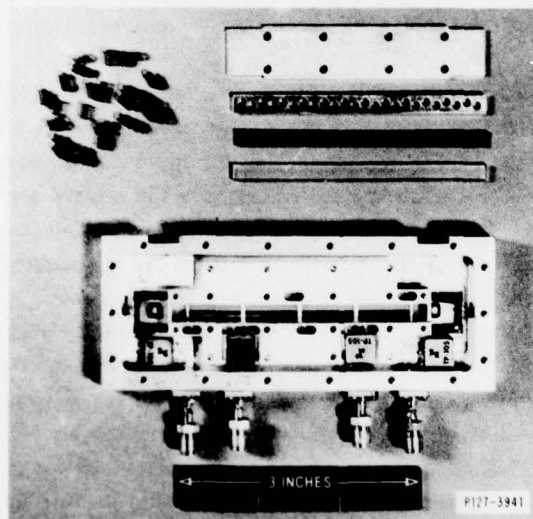


Fig. V-7. Partially assembled acoustoelectric device. Also shown are RTV pillow, beryllium-copper diaphragm, spring insert, springs and pressure plate which maintain a stable air gap during temperature fluctuations.

This assembly procedure achieves the desired features of cleanliness, accuracy, ease of assembly, and stability of the device structure with respect to stress and temperature variations. These features, in turn, help provide the near-ideal and reproducible electrical performance desired in acoustoelectric surface-wave devices.

S. A. Reible    R. L. Slattery  
H. I. Smith    I. M. Coates

### C. DEVELOPMENT OF AN ACOUSTOELECTRIC-MEMORY-CORRELATOR SUBSYSTEM

The acoustoelectric memory correlator is a surface-wave device which has undergone continuing development, and the feasibility of using such a device as a programmable matched filter has been demonstrated.<sup>4,11,12</sup> The memory correlator is a gap-coupled acoustoelectric device with a matrix of free-standing Schottky-barrier diodes on a silicon strip which is held in close proximity ( $\sim 0.3 \mu\text{m}$ ) to the surface of a  $\text{LiNbO}_3$  SAW delay line. The operation of a memory correlator involves first the storage of a reference signal, and subsequently the cross correlation of other signals with the stored reference.

The phase and amplitude of a reference surface wave launched into the delay line of a memory correlator are recorded as a spatially varying charge pattern on the diode matrix by applying a forward-bias voltage pulse across the composite Si- $\text{LiNbO}_3$  structure for a fraction of an RF cycle. Upon removal of the impulse, the charge induced on the diodes serves to self-reverse-bias the diodes, and the reference signal is retained as a spatially varying depth modulation of the depletion layer behind the diodes. The maximum storage time is determined by the diode leakage current.

During the time that the reference pattern is stored, a second signal may be launched into the delay line, where the piezoelectric fields of the second signal will interact with the spatially varying stored charge pattern of the reference signal. The resulting acoustoelectric voltage induced across the memory-correlator structure is the correlation between the second signal and the reference wave. The device then functions as a programmable matched filter, with the response determined by the stored reference wave.

The details of the basic mechanical assembly and the diode characteristics have been described previously.<sup>13,14</sup> In this report, we shall discuss some of the improvements that have been made to increase the level of performance and the development of a subsystem which incorporates the improved devices.

#### 1. Mechanical Structure

Proper operation of the memory correlator requires that a stable, uniform gap be maintained between the silicon and the  $\text{LiNbO}_3$  delay line. For the devices under development, this requires a spacing of  $0.35 \mu\text{m}$  with a uniformity of  $\pm 0.01 \mu\text{m}$  over an interaction region of  $1.9 \times 0.17 \text{ cm}$ . Previous devices have used a pseudorandom array of  $2\text{-}\mu\text{m}$ -diam posts which are generated as a relief pattern by ion-beam-etching the  $\text{LiNbO}_3$ . Studies of acoustoelectric devices have shown that the use of the posts results in some additional loss in the device due to the scattering of the propagating acoustic waves by the posts. An analysis of this problem has led to the use of long thin ( $\sim 3.5 \mu\text{m}$ ) ion-beam-etched rails as the support structure for the silicon strip. A detailed analysis of the transverse modes in rail structures has been performed and experimental studies have been made.<sup>15-18</sup> Indications are that the deleterious effects



caused by the existence of transverse modes can be minimized by employing a structure consisting of a rail at each edge of the acoustic beam and one in the center. This geometry provides the optimum combination of minimal perturbation of the propagating waves consistent with the desired mechanical rigidity. This structure is currently being used for the memory-correlator prototypes.

Another change was to increase the length of the  $\text{LiNbO}_3$  delay line in an attempt to reduce the direct electromagnetic feedthrough from the acoustic input port to the correlator output port. This yielded some improvement, and it was possible to obtain >95-dB isolation between the RF signal applied to the acoustic port and the electromagnetic (E-M) leakage appearing at the correlator output. This isolation did not prove to be sufficient, and additional alterations, which are described in the following section, improved this figure by an additional 20 dB.

## 2. $\text{LiNbO}_3$ Delay Line

The first prototype memory correlators were assembled with delay lines having a bandwidth of 25 MHz centered about 100 MHz.<sup>14</sup> To meet the requirements of an existing system, new devices were developed with a bandwidth of 60 MHz centered at 150 MHz. In addition to an improved transducer design, the delay lines also incorporated multi-strip couplers to separate the desired surface-wave signal from the spurious bulk waves which are also launched by the transducer. This separation is only partially successful because bulk waves diffract from the initial track into the offset track containing the silicon strip. These spurious signals interfere with the surface-wave signal during both the storing of the reference waveform and the correlation with the stored reference. The presence of the bulk waves results in unwanted and unpredictable spurious signals at the output.

To achieve an additional level of E-M feedthrough suppression, the input transducer is driven in a "balanced," or push-pull mode, as compared with the usual practice of connecting one side of the transducer to ground. When driven in this fashion, the transducer requires matched-tuning inductors to each side and an unbalanced-to-balanced transformer to convert the input RF signal. Though the matching is somewhat more involved because two inductors must be adjusted together, proper tuning results in virtually complete cancellation of the E-M feedthrough at the correlator output. Memory correlators using this balanced transducer design have been assembled, and any resulting E-M feedthrough is lost in the band-limited noise level of the output amplifier ( $\sim -92$  dBm) for input powers of up to +23 dBm.

## 3. Memory-Correlator-Subsystem Performance

The latest prototype memory correlators have been designed to act as programmable sub-pulse compressors in a radar burst-processor. The memory-correlators must be compatible with the remainder of the processor which is being developed by General Electric Company under contract to the U.S. Army. To facilitate the use of the memory correlator in this application and, at the same time, to provide a "stand-alone" unit which can be easily interfaced with other RF systems, a memory-correlator subsystem was designed and built. The block diagram of the subsystem is shown in Fig. V-8. The function of the subsystem is to receive the appropriate commands and generate the necessary chain of signals so that the memory correlator will store an externally supplied RF waveform as the reference, receive an externally supplied RF waveform at a later time to be correlated with the stored reference, and then



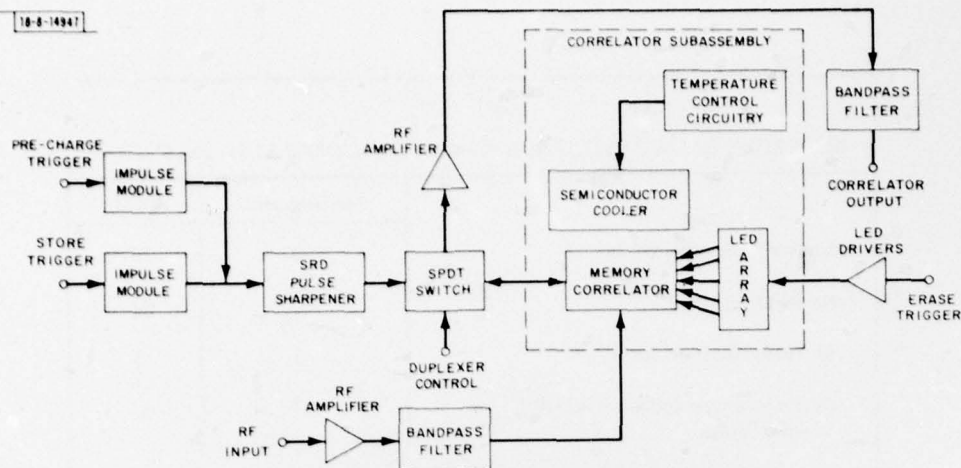


Fig. V-8. Block diagram of memory-correlator subsystem. Portion within dashed line is shown in Fig. V-9.

erase the stored reference with a flash of LED illumination prior to the next reference signal. The unit is completely self-contained and can either operate on a built-in clock for synchronism or be slaved to a master synchronization source. To prevent the heat buildup within the subsystem from degrading the storage time of the Schottky-barrier diodes, it is necessary to mount the memory correlator in an insulated chassis with a thermoelectric cooler. The interior of this chassis with a memory correlator in place and the temperature control board for the cooler is shown in Fig. V-9.

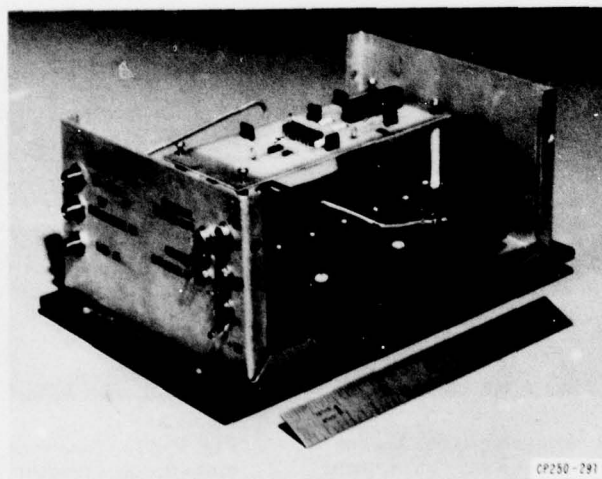
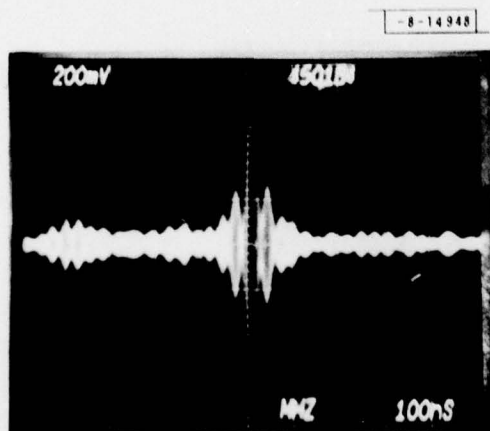


Fig. V-9. Memory correlator mounted on thermoelectric coolers with temperature control board.

TABLE V-2		
PROPERTIES OF ACOUSTOELECTRIC-MEMORY-CORRELATOR SUBSYSTEM		
	Achievement	Goal
Center Frequency (MHz)	150	150
Bandwidth (MHz)	60	60
RF Pulse Duration ( $\mu\text{sec}$ )	5	5
Dynamic Range (above kTB) (dB), 5- $\mu\text{sec}$ pulse <sup>†</sup>	50	>60
Amplitude Uniformity (dB)	$\pm 3$	$\pm 0.5$
Spurious Levels (related to output) (dB), 5- $\mu\text{sec}$ pulse <sup>†</sup>	-24	-35
<sup>†</sup> +23-dBm stored reference.		



V-10. Correlator output using 2- $\mu\text{sec}$ , MHz, linear-FM waveform as stored reference and signal. Horizontal scale is 100  $\mu\text{sec}/\text{div}$ .

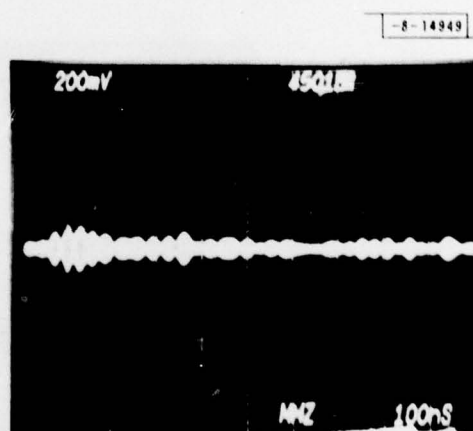


Fig. V-11. Spurious signals present in memory correlator when excited with 2- $\mu\text{sec}$ , 40-MHz, linear-FM waveform. Horizontal scale is 100  $\mu\text{sec}/\text{div}$ .

The current performance of the subsystem and the desired goals are shown in Table V-2. Figure V-10 shows the correlator output when using a 2- $\mu$ sec, 40-MHz, unweighted linear-FM waveform centered at 150 MHz for both the stored reference and the subsequent input signal. It can be seen that the spurious levels in the memory correlator are still much higher than desired. These spurious signals are primarily caused by detection of the surface acoustic wave by the edges of the silicon strip and by bulk waves within the interaction region. The level of these spurious signals can be seen in Fig. V-11, which shows the same 2- $\mu$ sec, 40-MHz, linear-FM waveform entered into the memory correlator, but without any stored reference. When a reference is stored, the spurious signals are more than 20 dB below the peak level of the desired output signal. These spurious signals scale linearly with signal power.

Design modifications to reduce spurious levels and to meet the goals for dynamic range on amplitude uniformity are in progress and will be reported at a later date.

D. H. Hurlburt	J. H. Cafarella
E. Stern	R. P. Baker
R. W. Ralston	



751 7030

# REFERENCES

1. An earlier version of the variable-bandwidth filter was described in Solid State Research Report, Lincoln Laboratory, M.I.T. (1976:4), pp. 71-73, DDC AD-A039175.
2. J. Melngallis, R. C. Williamson, and R. H. Domnitz, "Filter with Bandwidth Continuously Variable from 5 to 100 MHz," in 1977 Ultrasonics Symposium Proceedings (IEEE, New York, 1977), pp. 965-968.
3. V. S. Dolat and R. C. Williamson, "A Continuously Variable Delay-Line System," in 1976 Ultrasonics Symposium Proceedings (IEEE, New York, 1976), pp. 419-423, DDC AD-A040522/5.
4. R. W. Ralston, J. H. Cafarella, S. A. Reible, and E. Stern, "Improved Acoustoelectric Schottky-Diode/LiNbO<sub>3</sub> Memory Correlator," in 1977 Ultrasonics Symposium Proceedings (IEEE, New York, 1977), pp. 472-477.
5. See Sec. I-A, this report.
6. R. W. Ralston, D. H. Hurlburt, F. J. Leonberger, J. H. Cafarella, and E. Stern, "A New Signal Processing Device, the Integrating Correlator," in 1977 Ultrasonics Symposium Proceedings (IEEE, New York, 1977), pp. 623-628.
7. See Sec. IV-B, this report.
8. R. Jolly, Appl. Phys. Lett. 29, 525 (1976).
9. Solid State Research Report, Lincoln Laboratory, M.I.T. (1977:4), pp. 53-57, DDC AD-A052463.
10. S. A. Reible, J. H. Cafarella, R. W. Ralston, and E. Stern, "Convolver for DPSK Demodulation of Spread Spectrum Signals," in 1976 Ultrasonics Symposium Proceedings (IEEE, New York, 1976), pp. 451-455, DDC AD-A040519/1.
11. K. A. Ingebrigtsen, Proc. IEEE 64, 764 (1976), DDC AD-A028456/2.
12. E. Stern and R. C. Williamson, Electron. Lett. 10, 58 (1974), DDC AD-A001053/8.
13. Solid State Research Report, Lincoln Laboratory, M.I.T. (1975:1), p. 57, DDC AD-A009848/3.
14. Ibid. (1976:4), p. 73, DDC AD-A039175.
15. K. L. Wang, "Modal Analysis of SAW Convolver," Technical Report 526, Lincoln Laboratory, M.I.T. (13 January 1978).
16. S. A. Reible et al., "Transverse Modes in Gap-Coupled Surface Wave Devices," submitted to Applied Physics Letters.
17. Solid State Research Report, Lincoln Laboratory, M.I.T. (1977:4), p. 53, DDC AD-A052463.
18. Ibid. (1978:1), p. 59.

UNCLASSIFIED

SECURITY CLASSIFICATION OF THIS PAGE (When Data Entered)

REPORT DOCUMENTATION PAGE		READ INSTRUCTIONS BEFORE COMPLETING FORM
1. REPORT NUMBER ESD/IR-78-96	2. GOVT ACCESSION NO.	3. RECIPIENT'S CATALOG NUMBER 9
4. TITLE (and Subtitle) Solid State Research, 1978:2.		5. TYPE OF REPORT & PERIOD COVERED Quarterly Technical Summary 1 February - 30 April 1978
7. AUTHOR(s) Alan L. McWhorter		6. PERFORMING ORG. REPORT NUMBER 1978:2
		8. CONTRACT OR GRANT NUMBER(s) F19628-78-C-0002
9. PERFORMING ORGANIZATION NAME AND ADDRESS Lincoln Laboratory, M.I.T. P.O. Box 73 Lexington, MA 02173		10. PROGRAM ELEMENT, PROJECT, TASK AREA & WORK UNIT NUMBERS Program Element No. 65705F Project No. 649L
11. CONTROLLING OFFICE NAME AND ADDRESS Air Force Systems Command, USAF Andrews AFB Washington, DC 20331		12. REPORT DATE 15 May 1978
		13. NUMBER OF PAGES 76
14. MONITORING AGENCY NAME & ADDRESS (if different from Controlling Office) Electronic Systems Division Hanscom AFB Bedford, MA 01731		15. SECURITY CLASS. (of this report) Unclassified
		15a. DECLASSIFICATION DOWNGRADING SCHEDULE
16. DISTRIBUTION STATEMENT (of this Report) Approved for public release; distribution unlimited.		
17. DISTRIBUTION STATEMENT (of the abstract entered in Block 20, if different from Report)		
18. SUPPLEMENTARY NOTES None		
19. KEY WORDS (Continue on reverse side if necessary and identify by block number)		
solid state devices	photodiode devices	infrared imaging
quantum electronics	lasers	surface-wave transducers
materials research	laser spectroscopy	charge-coupled devices
microelectronics	imaging arrays	acoustoelectric devices
surface-wave technology		
20. ABSTRACT (Continue on reverse side if necessary and identify by block number)		
<p>This report covers in detail the solid state research work of the Solid State Division at Lincoln Laboratory for the period 1 February through 30 April 1978. The topics covered are Solid State Device Research, Quantum Electronics, Materials Research, Microelectronics, and Surface-Wave Technology. Funding is primarily provided by the Air Force, with additional support provided by the Army, ARPA, NSF, and DOE.</p>		

UNCLASSIFIED

SECURITY CLASSIFICATION OF THIS PAGE (When Data Entered)

207 650

LB